Highly active ZnO-based biomimetic fern-like microleaves for photocatalytic water decontamination using sunlight

Albert Serrà [l,*], Yue Zhang [&], Borja Sepúlveda [&], Elvira Gómez [$,@], Josep Nogués [&,#], Johann Michler [l], Laetitia Philippe [l,*]

[l] Empa Swiss Federal Laboratories for Materials Science and Technology, Laboratory for Mechanics of Materials and Nanostructures, Feuerwerkerstrasse 39, CH-3602 Thun, Switzerland.

[&] Catalan Institute of Nanoscience and Nanotechnology (ICN2), CSIC and BIST, Campus UAB, Bellaterra, E-08193 Barcelona, Spain.

[$] Grup d'Electrodeposició de Capes Primes i Nanoestructures (GE-CPN), Departament de Ciència de Materials i Química Física, Universitat de Barcelona, Martí i Franquès, 1, E-08028, Barcelona, Catalonia, Spain.

[@] Institute of Nanoscience and Nanotechnology (IN^{2}UB), Universitat de Barcelona, Barcelona, Catalonia, Spain.

[#] ICREA, Pg. Lluís Companys 23, E-08010, Barcelona, Spain.

* Corresponding authors: albert.serraramos@empa.ch (A.S.); laetitia.philippe@empa.ch (L.P.)

ABSTRACT: Here we present the highly enhanced sunlight photocatalytic efficiency and photocorrosion resistance of biomimetic ZnO-modified micro/nanofern fractal architectures, which are synthesized by using a novel, simple, inexpensive and green electrochemical deposition approach in high stirring conditions. Such fern-like hierarchical structures simultaneously combine enhanced angle independent light trapping and surface/bulk modifications of the ZnO morphology to drastically increase: i) the light trapping and absorption in the visible near-infrared range, and ii) the surface to volume ratio of the architecture. This combination is crucial for boosting the sunlight photocatalytic efficiency. To modulate the electronic properties for extending the operation of the ZnO photocatalysts into the visible domain we have used three different modification approaches: sulfidation (leading to a ZnS shell), Ag decoration, and Ni-doping. The different ZnO-modified bioinspired fern-like fractal structures have been used to demonstrate their efficiency in the photodegradation and photoremediation of three different persistent organic pollutants –methylene blue, 4-nitrophenol, and Rhodamine B – under UV light, simulated and natural UV-filtered sunlight. Remarkably, the ZnO@ZnS core@shell structures exhibited

an outstanding photocatalytic activity compared to the pristine ZnO catalyst, with over 6-fold increase in the pollutant degradation rate when using solar light. In fact, the catalytic performance of the ZnO@ZnS micro/nanoferns for the photoremediation of persistent organic pollutants is comparable to or better than the most competitive state-of-the-art ZnO photocatalysts, but showing a negligible photocorrosion. Ag-decorated ZnO, and Ni-doped ZnO exhibited similar excellent visible-sunlight photodegradation efficiency. Although the Ni-doped photocatalysts showed a relatively poor photocorrosion resistance, it was acceptable for Ag-decorated ZnO. Therefore, the easy fabrication and the capacity to drastically enhance the sunlight photocatalytic efficiency of the ZnO@ZnS bioinspired micro/nanoferns, together with their practically negligible photocorrosion and simple recyclability in terms of non-catalyst poisoning, makes them very promising photocatalysts for water remediation.

Graphical Abstract

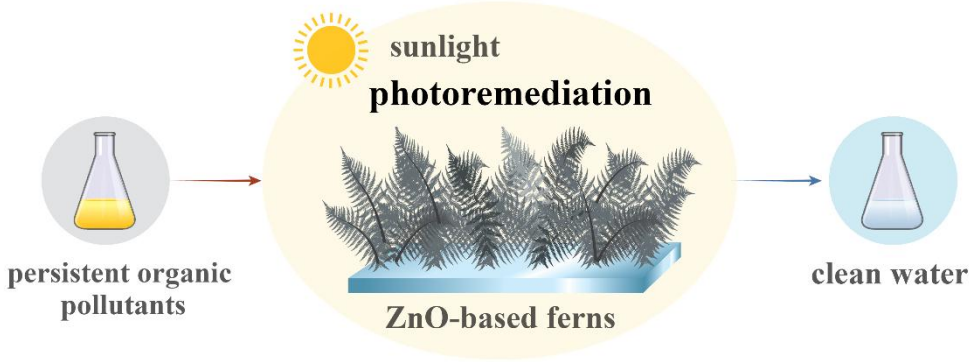

Highlights

- Simple electrosynthesis of biomimetic micro/nanofern fractal structures as enhanced sunlight photocatalysts is stablished.
- Efficient sulfidation, photodeposition or codeposition ZnO modification approaches are proposed for tuning ZnO electronic properties to enable visible light absorption.
- Enhanced visible light trapping by the fractal geometry and the surface/bulk electronic modifications in the ZnO enables boosting the sun light photocatalytic efficiency.

- ZnO@ZnS, Ag-decorated ZnO and Ni-doped ZnO show excellent photodegradation and photoremediation efficiencies of persistent organic pollutants under sunlight irradiation.

- ZnO@ZnS core@shell micro/nanoferns exhibit excellent photocatalytic activity, photocorrosion resistance and recyclability.

KEYWORDS: sunlight photocatalysis; biomimetic; bioinspiration; persistent organic pollutants; electrodeposition.

1. INTRODUCTION

In September 2015, the United Nations held a summit regarding the sustainable development of the planet, wherein representatives from social, political, scientific, and private sectors drew up a fifteen-year agenda containing seventeen Sustainable Development Goals (SDG). In the context of sustainable development, a specific goal pertaining to water and sanitation (SDG6), with the objective to "ensure availability and sustainable management of water and sanitation for all," has become a forefront societal issue. At present, more than 40% of the world's population is affected by water scarcity, a number that has been predicted to increase due to global warming and anthropogenic activities [1-3]. The protection and recovery of aqueous ecosystems and the development of effective water decontamination technologies are therefore imperative.

Water can be threatened mainly by pathogens (e.g. bacteria), inorganic materials (e.g. heavy metals), organic compounds (e.g. persistent organic pollutants), and macroscopic pollutants (e.g. plastics) [4, 5]. Currently, conventional water treatment technologies are insufficient for eliminating certain chemicals, such as persistent organic pollutants [6-8]. In order to remove these substances, advanced oxidation processes (e.g. Fenton, photofenton, and photocatalysis, among others) are the most widely investigated technologies [8-11]. Recently, nano/micromaterials have been extensively studied as powerful tools for implementing new green and sustainable materials for the development of advanced oxidation processes, especially in photocatalysis [10-13]. Photochemistry is a highly promising approach as it uses solar light (it must be noted that solar light consists of ~5% UV, ~43% visible, and ~52 % infrared) as

a renewable, abundant, and clean energy source [14-16]. In this sense, semiconducting materials, such as ZnO, TiO_2, V_2O_5, and Nb_2O_5, have been recently proposed as efficient photocatalysts for the photodegradation of persistent organic pollutants [17-19]. Among these photocatalysts, ZnO is one of the most fascinating semiconductors as a result of its chemical stability, low toxicity, piezoelectricity, light conversion efficiency, antibacterial and antifungal activity, and high activity with regard to the production of reactive oxygen species (ROS) under UV light [19-23]. Moreover, ZnO can be easily prepared using simple and scalable approaches in a wide variety of morphologies, architectures, and shapes, including nanowires, nanorods, nanoparticles, urchins, and nanosprings, among others [19-23]. However, it shows limited photocatalytic activity when sunlight is used because of its wide band gap (3.36 eV), which requires an excitation wavelength in the UV domain ($\lambda < 390$ nm) [19-24]. During the last few decades, it has been demonstrated that the recombination rate of photogenerated holes and electrons is a key factor that determines the photocatalytic activity, as it reduces the quantum yield and causes energy wasting [19-24]. Therefore, the successful band gap modulation of ZnO photocatalysts by, for example, doping is required to minimize the recombination losses of charge carriers and to extend the light response to visible light. In this regard, different doping, thin film deposition, implantation, or nanoparticle deposition strategies have been used to enhance the photocatalytic activity of ZnO: (i) Anionic doping (e.g. C, N, and S); (ii) cationic doping (e.g. Al, Sb, Mn, Ni, Co, Bi, Fe, K, and Mg); (iii) rare earth doping (e.g. Ce, Dy, Er, Eu, Gd, Ho, and Nd); (iv) co-doping; and (v) semiconductor coupling [25-27]. It is well known that doping can increase carrier mobility and reduce the recombination *via* separation of photogenerated electron and holes. In addition, surface decoration with metal nanostructures can, on the one hand, improve the trapping of photogenerated carriers at the surface and, on the other hand, amplify light absorption by exploiting their localized surface plasmon resonance, thereby enabling enhanced photocatalytic efficiency with visible light. For example, C-doped ZnO porous structures, Mg-doped ZnO nanoparticles, Fe-doped ZnO nanofibers, Eu-doped ZnO nanoparticles, and Er-Al co-doped nanoparticles showed enhanced photocatalytic performance towards various pollutants under visible light [28-32]. In addition, core@shell semiconductor heterojunctions have also recently been proven to enhance the charge separation of electron-hole pairs and, consequently, the photocatalytic efficiency. In addition, the formation of two-phase heterojunctions can extend light absorption to the visible domain

due to the induced mechanical stress and to the creation of impurity energy levels within the band gap. For example, ZnO@ZnS core@shell nanorods have been studied as photocatalysts for methylene blue (MB) and Rhodamine-B (Rh-B) mineralization under visible light [23]. Core@shell structures have also been proven to increase the photo-stability and photocorrosion resistance of ZnO in aqueous solution, which dramatically limits the usage of ZnO structures in water decontamination using sunlight [23, 33, 34]. In addition, doping with magnetic transition metals (e.g. Ni, Co, and Fe) has also been demonstrated to be an excellent strategy to recover and recycle the photocatalysts and enhance the catalytic activity through the convection of catalysts during the reaction under the application of magnetic fields [35, 36].

Finally, the shape and architecture of the photocatalysts have also been shown to be a determinant factor controlling the photocatalytic activity due to the active surface to trap light and pollutants, i.e. leading to more efficient photocatalysis [37, 38]. In this sense, it is worth noting that nature already offers efficient photochemistry architectures or shapes (i.e. in plants, animals, and microorganisms, among others). Nature offers hierarchical architectures with multilevel light scattering, high electron-diffusion length, open and accessible porosity, high surface-to-volume ratios, and high light absorption independent from incident light angle, among other important characteristics for photochemistry. It is well known that human-made materials have been unable to compete with nature in general [39-42]. It is, therefore, a smart strategy to synthesize bioinspired materials to develop more efficient and competitive materials. In this regard, ZnO biomimetic materials, such as sea urchins or bioinspired nanoparticles, have been demonstrated to be efficient photocatalysts for solar cells or water decontamination due to the improved light trapping and easily pollutant accessibility [22, 26, 43, 44]. Among the different possible architectures, it is well known that fern leaves, due to their hierarchical, fractal, structure, [45] are extremely efficient platforms for biological processes such as photosynthesis. By extension, human-made fern-like leaves have been investigated as efficient nitroaniline chemical sensors, solar energy storage and photocatalysts for water decontamination and hydrogen production [46-50]. In previous studies researchers suggested that the branched architecture of micro/nanoferns is responsible for optimal photochemical performance, however, the reason of these improvements is not shown.

Here, we have developed a facile and scalable multi-step approach for the electrosynthesis of supported micro/nanofern hierarchical structures with ZnO electronic modifications to increase sun light photocatalytic efficiency and improve photocorrosion resistance. To achieve this goal, ZnO, ZnO@ZnS core@shell, ZnO modified by Ag photodeposition, and Ni-doped fern-like bioinspired fractals have been successfully synthesized in a simple, cost-effective, efficient and fast manner via electrodeposition. In this work, we have shown that fractal and dendritical architectures of micro/nanoferns allow to increase the surface to volume ratio, which is extremely important for heterogeneous catalysis. Additionally, we have demonstrated, for the first time, that micro/nanofern architectures are responsible for the excellent photochemical properties of fern-like materials as a consequence of the high light absorption independent from incident light angle, which offers greater light trapping and light harvesting capacities compared to other architectures. Moreover, the effect on micro/nanofern fractal architecture (i.e. light trapping and light harvesting capacities) of three different modification approaches used to modulate the electronic properties of ZnO-based photocatalysts was discussed. The morphology, crystallographic and electronic structure, as well as optical, photoelectrochemical and electrical properties of each photocatalyst was investigated. The efficiency of the fabricated bioinspired structures was tested by analyzing the degradation kinetics of MB, 4-nitrophenol (4-NP), and Rh-B persistent organic pollutants under UV, simulated and natural UV-filtered sunlight irradiation. Ag-decorated and Ni-doped ZnO micro/nanoferns exhibit better photocatalytic activity in the visible range than pure ZnO structures. In contrast, the ZnO@ZnS core@shell micro/nanoferns present an excellent photocatalytic activity using sunlight, with a performance comparable to, or better than that of benchmark materials reported in literature. This fact, combined with their exceptional photo-stability and photocorrosion resistance, makes them optimum candidates for "green" photocatalytic water remediation purposes using sunlight.

EXPERIMENTAL SECTION

1.1. Electrodeposition of branched-ZnO nanorod arrays

ZnO micro/nanofern arrays were fabricated by electrochemical deposition, using a classical three-electrode electrochemical cell, from 0.5 mM $ZnCl_2$ (Fluka, > 98.0 %) + 0.1 M KCl (Sigma, > 99.0 %) oxygen

saturated (bubbled 45 min before and during the electrodeposition) aqueous solution (pH = 7 in standard conditions) maintained at 80 °C. Linear sweep voltammetry experiments were performed on conductive fluorine-doped tin oxide films on a glass substrate at 80 °C in order to select the most adequate potential. The electrochemical growth was performed under magnetic stirring (silent and 400 rpm) conditions using a rod stirrer placed in the center of the cell. The electrodeposition was carried out potentiostatically at –1.0 V with a 28 C cm^{-2} charge density using an Autolab with a PGSTAT30 potentiostat/galvanostat and the NOVA software. The working electrodes were fluorine-doped tin oxide films on glass substrates. Fluorine-doped tin oxide electrodes were cleaned in acetone, ethanol, and water and then air dried prior to the immersion in the solution. The counter and reference electrodes were a Pt mesh and Ag/AgCl/KCl (3 M) electrode, respectively. After the electrodeposition, the ZnO micro/nanofern arrays were cleaned exhaustively with distilled water, dried at room temperature, and then annealed for 2 h at 400 °C in an argon atmosphere. The annealing treatment was performed using rapid thermal annealing equipment (Advanced Riko Mila 5050). The heating ramp rate was set to 10 °C min^{-1}.

1.2. Preparation of modified branched-ZnO nanorod arrays

Sulfidation, photodeposition, and co-deposition were used to fabricate ZnO@ZnS core@shell, ZnO decorated with Ag, and Ni-doped branched-ZnO nanorod arrays, respectively (see **Figure 1**):

(i) ZnO@ZnS core@shell: The as-electrodeposited ZnO micro/nanofern arrays (without annealing treatment) were immersed in an aqueous solution of 30 mM thioacetamide—CH_3CSNH_2—(Sigma-Aldrich, 98%) at 40 °C in a water bath for 4 h. The samples were then washed with water and ethanol, dried at room temperature, and annealed for 2 h at 400 °C in an argon atmosphere.

(ii) ZnO modified by Ag decoration: The annealed ZnO micro/nanofern arrays were immersed in an aqueous solution of 0.75 mM $AgNO_3$ (Sigma-Aldrich, > 99.0 %) at room temperature. The deposition was carried out by two UV lamps (365 nm; nominal power of 5 W, light intensity of 79.3 ± 0.9 lux) focused on the annealed-ZnO branched nanorod arrays' surface for 60 min. Note that the solutions were bubbled with nitrogen for 30 min prior to and during the photodeposition of Ag.

(iii) Ni-doped branched-ZnO by co-deposition: Ni-doped ZnO micro/nanofern arrays were prepared through electrochemical co-deposition from 0.5 mM $ZnCl_2$ (Fluka, > 98.0 %) + 0.005 mM $NiCl_2$ (Sigma-Aldrich, > 98 %) + 0.1 M KCl (Sigma, > 99.0 %) oxygen saturated (bubbled 45 min before and during the electrodeposition) aqueous solution (pH = 7 in standard conditions) maintained at 80 °C under magnetic stirring (400 rpm) conditions. The electrochemical growth was performed potentiostatically at –1.0 V to attain 28 C cm^{-2} charge density using an Autolab with a PGSTAT30 potentiostat/galvanostat and the NOVA software. The samples were washed with water and ethanol, dried at room temperature, and annealed for 2 h at 400 °C in an argon atmosphere.

1.3. Characterization of the photocatalysts

Different characterization techniques were used to analyze the ZnO and ZnO-modified micro/nanofern arrays photocatalysts. The surface morphologies were analyzed by field-emission scanning microscopy (FE-SEM, Hitachi S-4800) equipped with an energy-dispersive X-ray spectroscopy (EDX) detector. In order to enhance the image definition and quality, prior to the SEM observation, 4 nm of Au was deposited onto each sample using a sputtering system (Leica EM ACE600). In addition, EDX elemental mappings were carried out on the pristine (i.e., without Au capping) ZnO@ZnS core@shell and Ag-decorated ZnO micro/nanoferns using a FEI Magellan 400L XHRSEM equipped with an Oxford Instruments Ultim Extreme EDX detector system. The elemental compositions were also estimated by X-ray fluorescence (XRF, Fischerscope® X-RAY XDV®-SDD). The specific surface area of each biomimetic photocatalyst was determined based on the Brunauer–Emmett–Teller (BET) method from N_2 adsorption-desorption isotherms at 77 K using a Micrometrics Tristar-II. The structural characterization was carried out using X-ray diffraction (XRD, Bruker D8 Discovery diffractometer) in the Bragg–Brentano configuration with CuK_α radiation. The surface chemical states of each sample were determined using X-ray photoelectron spectroscopy (XPS) at room temperature with a SPECS PHOIBOS 150 hemispherical analyzer (SPECS GmbH, Berlin, Germany) in a base pressure of $5 \cdot 10^{-10}$ mbar using monochromatic Al Kalpha radiation (1486.74 eV) as the excitation source. The optical and electrical properties of the photocatalysts were analyzed by recording the UV-visible diffused reflectance spectra (DRS), photoluminescence spectra (PL), and Fourier-transform infrared spectra (FTIR). The DRS were measured using

a UV-visible PerkinElmer Lambda 900 UV spectrophotometer (PerkinElmer). The PL spectra were collected using a custom made set up, composed of an LED source with emission at 365 nm (M365FP1, Thorlabs), which was bandpass filtered (FB360-10, Thorlabs) for excitation. The backscattered PL was long-pass filtered (FEL0400, Thorlabs) and it was detected with an Andor 193i spectrometer equipped with an Andor Idus camera. The FTIR spectra were registered using a Perkin Elmer Spectrum 2 IR (Perkin Elmer). The photocurrent experiments were performed in an Autolab with a PGSTAT30 potentiostat–galvanostat and the NOVA software using a three-electrode system, with a Pt wire as the counter electrode, a Ag/AgCl/KCl (3 M) electrode as a reference and the as-prepared photocatalysts as the working electrode. The electrolyte used for all electrochemical measurements was a 0.5 M Na_2SO_4 aqueous solution (pH 6.8). Amperometric photocurrent (j–t) curves were recorded at 0.1 V versus the Ag/AgCl/KCl (3 M) electrode under artificial UV-filtered sunlight in 30-s on–off cycles. In addition, to evaluate the effect the angle of the incident light on the photocurrent, three different incident irradiation angles (30^o, 90^o, and 150^o) were used.

1.4. Photocatalytic and photocorrosion resistance tests

The photocatalytic activity of the different photocatalysts was tested by monitoring the decomposition of 10 ppm MB (Sigma-Aldrich, > 97 %), 10 ppm 4-NP (Fluka, > 99 %), and 5 ppm Rh-B (Sigma-Aldrich, > 98 %) pollutants under: (i) an 8 W mercury lamp setup with the wavelength of 365 nm (light intensity of 345 ± 3 lux); (ii) a 75 W Xe lamp setup with UV-filtered simulated sunlight (light intensity of 700 ± 18 lux); and (iii) natural UV-filtered sunlight (average light intensity 1400 ± 350 lux). The light intensity was measured every 15 min, always set in the position of maximum intensity using an Urceri MT-912 Digital Lux meter. Long-pass filters (cut-on wavelength region: 400 nm to 2200 nm) were introduced to limit the wavelength radiation and avoid direct photolysis of the pollutants, following the recommendations given by the International Organization for Standardization (10678:2010 standard).

In a typical photocatalytic test, 1 cm^2 of ZnO or modified-ZnO micro/nanoferns photocatalysts were immersed in 10 mL of pollutant solution with an initial concentration of 10 ppm MB (pH=8), 10 ppm 4-NP (pH=9), or 5 ppm Rh-B (pH=8). These solutions were first kept in dark conditions for 60 min to

reach the adsorption-desorption equilibrium prior to irradiation. The photocatalysis for each pollutant was conducted under argon bubbling at room temperature (25 °C). In addition, pollutant solutions without any photocatalysts were subjected to the same treatment as the control test. The photodegradation of each pollutant was followed by the reduction in the maximum absorption peak intensity of MB, 4-NP, and Rh-B at 662 nm, 400 nm, and 554 nm, respectively, in the three different illumination conditions: (i) UV light, (ii) artificial UV-filtered sunlight, or (iii) natural UV-filtered sunlight for an overall time of 120 min. The temporal evolution of the photocatalytic reaction was tracked *ex-situ* by UV-visible spectroscopy in a quartz cuvette with an optical length of 1 cm using a UV-1800 Shimadzu UV-vis spectrophotometer (Shimadzu Corporation). Then, the photocatalytic activity of the photocatalysts was calculated as a function of A_t/A_0, where A_0 is the absorbance of the maximum absorption peak of the test solution of each pollutant before irradiation and A_t is the absorbance in the maximum absorption peak of each pollutant after the irradiation time (t). The photodegradation efficiency ($A_{120\ min}/A_{0\ min}$) of each pollutant solution was also measured for five consecutive cycles, after 1, 6, 15, 30, and 48 h of continuous irradiation (artificial UV-filtered sunlight) in fresh water, to test the photo-stability, photo-corrosion resistance, and reusability of the photocatalysts. In addition, the photostability and photocorrosion resistance were also examined by the determination of the Zn(II) concentration in aqueous media after 1, 6, 15, 30, and 48 h of continuous irradiation (UV and artificial UV-filtered sunlight) in fresh water by a spectrophotometric method using Zincon monosodium salt (Sigma-Aldrich) in borate buffer (50 mM, pH=9). The absorbance at 620 nm, associated to the Zn(II)-bound Zincon complex, was measured in a quartz cuvette with an optical length of 1 cm using a UV-1800 Shimadzu UV-vis spectrophotometer (Shimadzu Corporation) to determine the amount of dissolved Zn [51]. Moreover, the total organic content (TOC) was determined to evaluate the mineralization efficiency (i.e. degradation of organic pollutants into intermediate compounds and subsequently, into CO_2 and H_2O). Note that prior to determining the TOC values, the samples were acidified with sulfuric acid and gasified to purge the CO_2 generated from the inorganic carbon. The TOC measurements were recorded using the high temperature combustion method on a catalyst (Pt-Al_2O_3) in a tubular flow microreactor operated at 680 °C, with a stream of hydrocarbon free air to oxidize the organic carbon, using a TOC-VCSN equipment

(Shimadzu) with a high sensibility column. Reproducible TOC values were always obtained using the standard NPOC (Non-Purgeable Organic Carbon) method.

1.5. Reactive oxygen species identification

The determination of the formation of hydroxyl radicals, oxygen superoxide, and singlet oxygen by the ZnO-based photocatalysts was studied under artificial UV-filtered sunlight ($\lambda > 400$ nm, light intensity of 700 ± 18 lux) by using chemical selective radical quenchers. The kinetics and concentration of hydroxyl radicals were measured by the time-dependent reduction of the fluorescence peak of fluorescein sodium salt – 8 µM of fluorescein sodium salt (Sigma-Aldrich) in aqueous solution – at 515 nm (λ_{ex} = 303 nm), due to its selective reaction with hydroxyl radicals. To determine the concentration of fluorescein sodium salt, a calibration curve was necessary, which involved comparing the unknown concentration to a set of standard samples of known concentrations. The reaction was followed by the fluorescence emission and the excitation spectra (λ_{ex} = 303 nm) using an AMINCO-Bowman Series 2 spectrofluorometer with a quartz micro-cell (1 mL) at 25 °C. The oxygen superoxide formation was monitored by measuring the time-dependent absorbance of the characteristic absorption peak of XTT-formazan at 475 nm, resulting from the reduction of a 100 µM aqueous solution of the XTT sodium salt (Sigma-Aldrich) by the oxygen superoxide. The oxygen singlet was determined by using the highly selective Singlet Oxygen Sensor Green reagent (Invitrogen) by measuring the reduction in the absorbance peak of a 5 mM methanol solution at 517 nm, due to the highly selective reaction between the anthracene part of this reagent and the singlet oxygen [52]. A quartz cuvette with an optical length of 1 cm using a UV-1800 Shimadzu UV-vis spectrophotometer (Shimadzu Corporation) was used to determine both oxygen superoxide and singlet oxygen formation. In addition, for identifying the ROS species during the photocatalysis, a pollutant solution of 10 ppm MB was used as an indicator, in which 1 mM isopropyl alcohol (Sigma-Aldrich, > 99.7%) (a quencher of hydroxyl radicals), 1 mM benzoquinone (Sigma-Aldrich, > 98%) (a quencher of superoxide radicals), or 1 mM triethanolamine (Sigma-Aldrich, > 99%) (a quencher of holes) were added. Then, the maximum absorption peak intensity of MB 662 nm after 120 min of artificial UV-filtered sunlight irradiation was measured.

2. RESULTS AND DISCUSSION

2.1. Photocatalyst synthesis and characterization

As can be seen in the schematic representation of the synthesis of ZnO and modified-ZnO micro/nano-fern arrays (**Figure 1**), the first step is always the electrochemical growth of ZnO or Ni-doped ZnO branched-nanorod arrays on the fluorine-doped tin oxide substrates. To select the most adequate potential, linear sweep voltammetry studies on the deposition solutions, both in deaerated and in oxygen-saturated conditions, have been performed, using the fluorine-doped tin oxide film on glass as a substrate from 0 to –1.5 V (vs. Ag/AgCl/KCl (3 M) reference) at 20 mV s^{-1}. The linear sweep voltammetry of the ZnO deoxygenated solutions allows the detection of a clear reduction peak (cathodic onset approximately at –1.12 V), corresponding to the Zn(II) reduction (**Figure S1**). However, the Zn(II) reduction peak could not be clearly identified when oxygen-saturated solutions were used as the oxygen reduction to form hydroxyl anions (cathodic onset around –0.76 V), overlaps with the Zn(II) reduction contribution as the anodic sweep reveal. In these conditions, some zinc was also electrodeposited (**Figure S1b**). In all cases, the abrupt increase in current at more negative potentials, irrespective of the solution and conditions, corresponds to massive hydrogen evolution. These results agree fairly well with the reported values for the electrochemical growth of ZnO nanorod arrays on fluorine-doped tin oxide substrates using chloride solutions [53-55]. To grow Ni-doped ZnO micro/nanofern arrays, Ni(II) chloride salt (0.005 mM $NiCl_2$) was added to the deposition solution. To clearly identify the electrodeposition of Ni(II), the same solution without Zn(II) chloride was also analyzed. As can be seen in the inset of **Figure S1b**, a clear Ni(II) reduction peak (cathodic onset approximately at –0.74 V) was detected (**Figure S1a**). A similar peak was also detected in the Ni-doped ZnO deoxygenated solution. However, this reduction peak cannot also be detected in oxygen-saturated conditions because of the initial oxygen reduction. From the detailed linear sweep voltammetric study, the electrodeposition of the branched-ZnO or the branched Ni-doped ZnO nanorod arrays was performed at –1 V with a continuous high flux of O_2 (6 L min^{-1}) and magnetic stirring (400 rpm) during the electrodeposition.

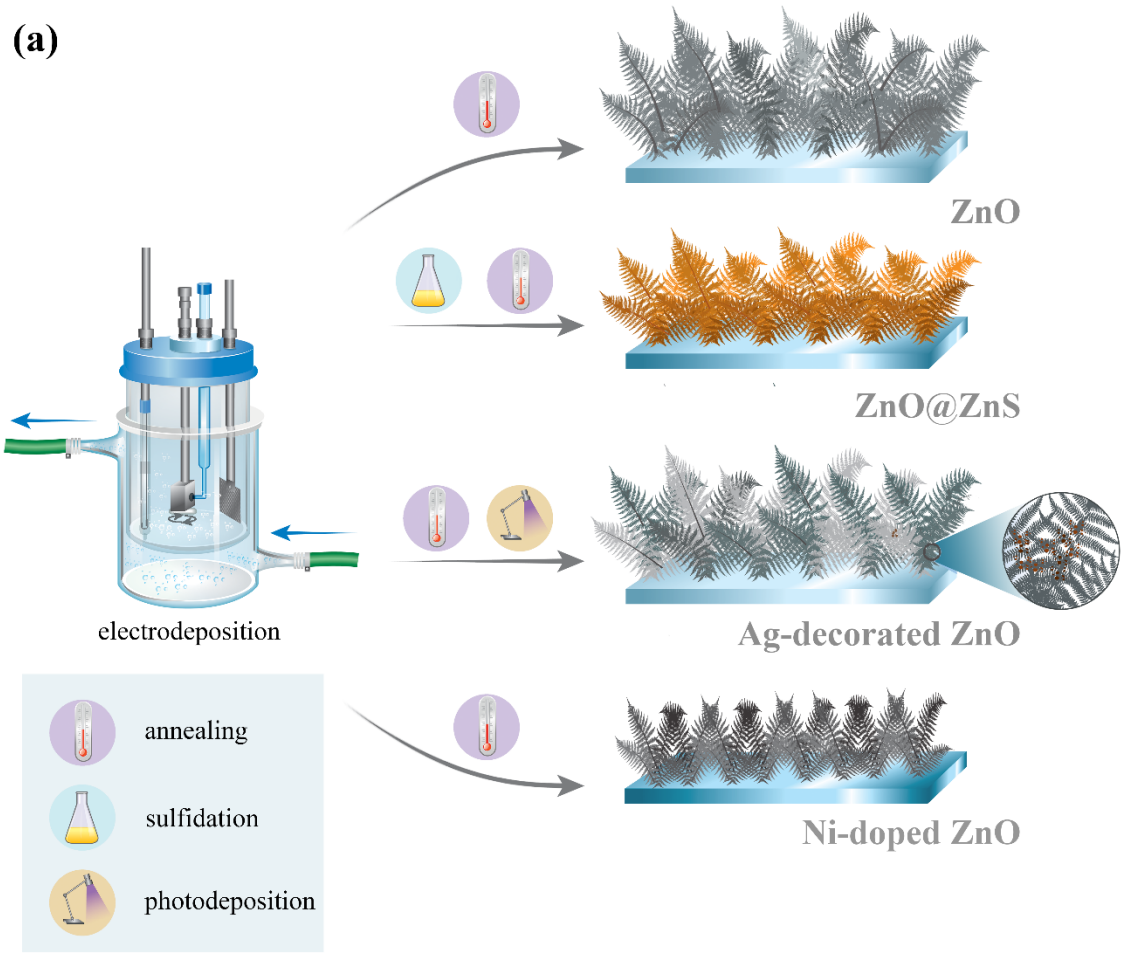
(a)
ZnO
ZnO@ZnS
Ag-decorated ZnO
Ni-doped ZnO
electrodeposition
annealing
sulfidation
photodeposition

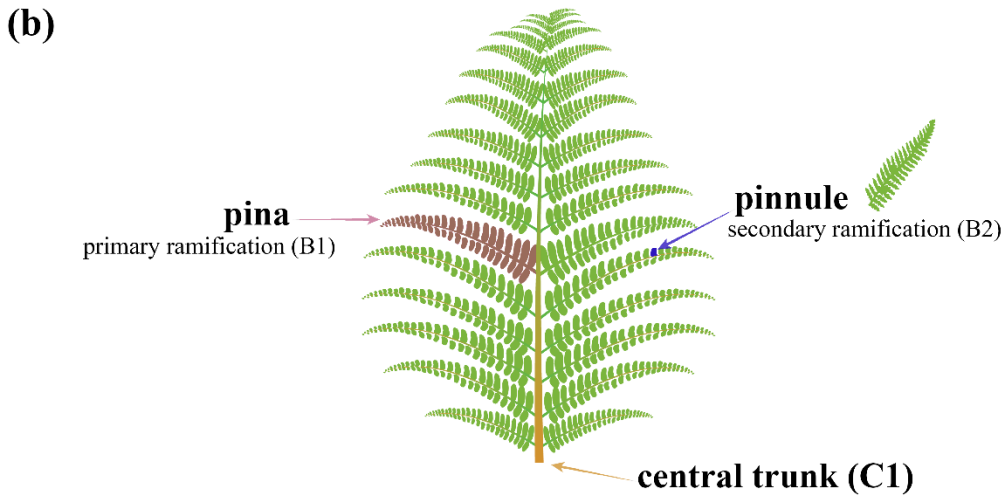
(b)
pina
primary ramification (B1)
pinnule
secondary ramification (B2)
central trunk (C1)

Figure 1: (a) Schematic representation of the electrochemical synthesis of the ZnO, ZnO@ZnS core@shell, ZnO modified by Ag decoration, and Ni-doped ZnO bioinspired fern-like leaf shape photocatalysts. (b) Schematic representation of the bioinspired fern micro-leaf indicating the different parts of micro/nanoferns used to label different elements of the microstructure, i.e., central trunk (C1), pinna - primary ramification (B1), and pinnule - secondary ramification (B2).

The FE-SEM images for all the samples show a dendritic microstructure resembling a bioinspired fern-like leaf shape (**Figure 2)** with different textures and dimensions (**Table 1**). In general, each fern-like micro-leaf is made up of a central trunk, where different pinna form (i.e., primary ramification), which in turn are characterized by small pinnules (secondary ramification). For the basic ZnO structures, the average size of the central trunk (C1 in Figure 1) is around ~1.2 µm in diameter and ~53 µm in length, whereas the average diameter of the branched nanorods (primary branching; B1 in Figure 1) is around ~500 nm, with small nanorods (secondary branching; B2 in Figure 1) with an average diameter of ~250 nm. The electrodeposition mechanism of ZnO nanorods using a Zn(II) chloride salt on conductive glass has been discussed in the literature [53-55]. According to these studies, the aspect ratio of the as-electrodeposited nanorods depends mainly on the relative concentration of Zn(II) with respect to [OH^-], since the kinetics of the ZnO precipitation is very fast [53-55]. The nanorod shape is attained when the OH^- electro-generation (controlled by the applied potential) is much faster than the mass transport of Zn(II) as a consequence of precipitation of the majority of Zn(II) that arrive at the electrode with hydroxide ions adsorbed on the tips. This subsequently facilitates the growth along the longitudinal axis and hinders it along the lateral directions. Consequently, the growth mechanisms depend on: (i) OH^- generation rate; (ii) mass transport (e.g. thermal and chemical diffusion and forced diffusion by the action of external forces); (iii) bath composition; (iv) surface conductivity; and (v) external distortions that occur because of the action of high external forces (e.g. magnetic stirring and very high oxygen bubbling). In the present study, the strong-stirring conditions bring about a continuous distortion in the precipitation process, which maintains the preferred growth along the longitudinal axis and facilitates the formation of discrete nucleus (non-continuous lateral growth) along the lateral surface of nanorods. In these nuclei, the longitudinal growth is preferred and the formation of discrete nuclei along the lateral

surface is also observed, resulting in branched nanorods. Notably, both magnetic and gas stirring are very relevant for the synthesis of fern-like microleaves, as the as-electrodeposited structures in non-magnetic stirring conditions (**Figure S2a**) showed a clear reduction in ramification (B2 in Figure 1), and an improvement in the continuous lateral growth of principal branches (B1 in Figure 1)—with diameters of around 20% greater. In addition, in non-magnetic stirring and a low continuous flux of O_2 (0.5 L min^{-1}), non-branched nanorods are obtained (**Figure S2c**).

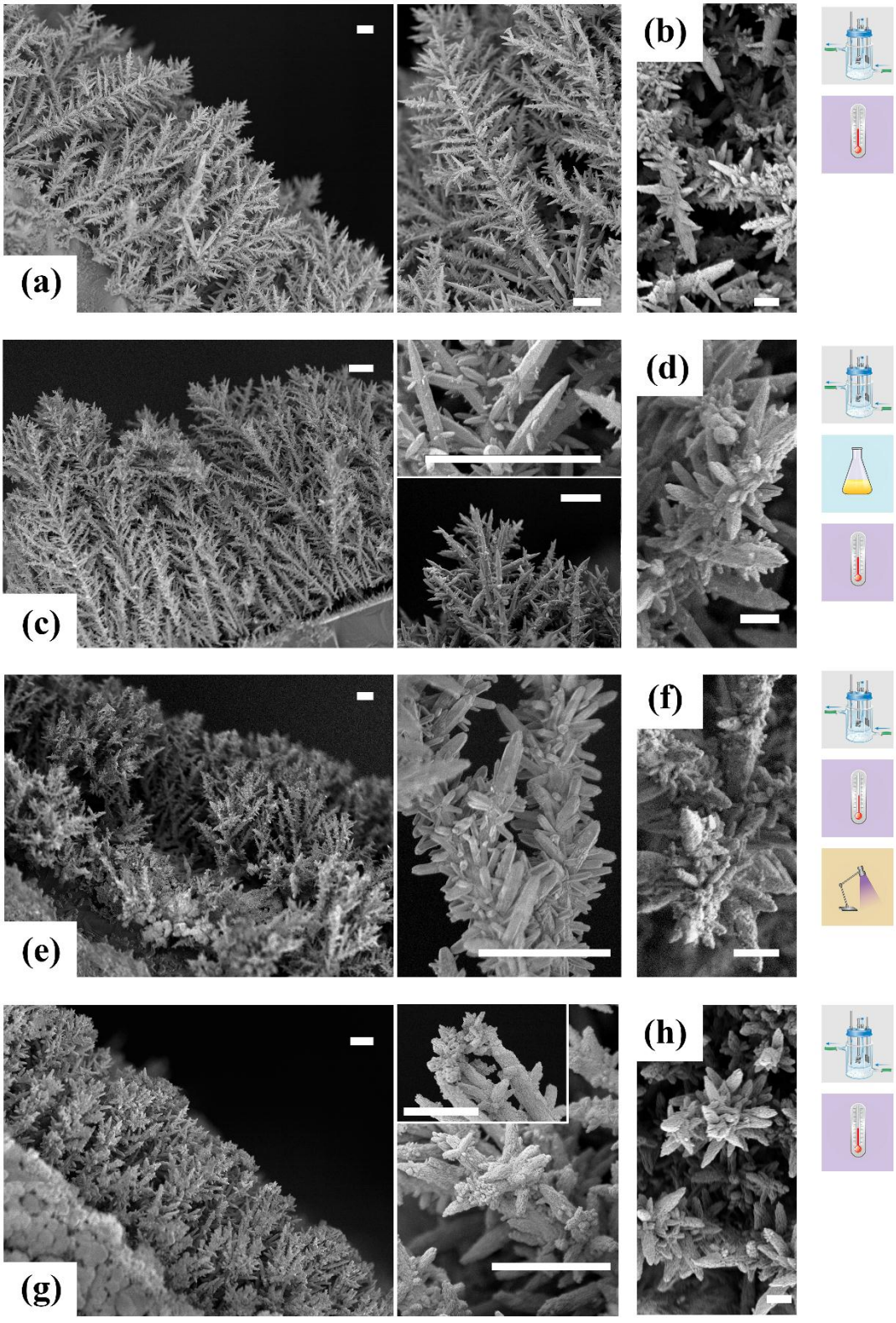

Figure 2: FE-SEM micrographs of fern-like bioinspired microleaves of (a: cross section and b: top view) ZnO, (c: cross section and d: top view) ZnO@ZnS core@shell, (e: cross section and f: top view) ZnO

modified by Ag NP decoration, and (g: cross section and h: top view) Ni-doped branched-ZnO by co-deposition. Scale bars: 5 µm (a, c, e, and g) and 1 µm (b, d, f, and h).

	ZnS, Ag or Ni to ZnO / at. %	Length of central stipe (C1) / µm	Diameter of central stipe (C1) / µm	Length of primary branches (B1) / µm	Diameter of primary branches (B1) / µm	Length of secondary branches (B2) / µm	Diameter of secondary branches (B2) / µm	BET surface area / $m^2\ g^{-1}$
ZnO	-	50–56	1.2 ± 0.2	2.7–7.3	0.50 ± 0.06	0.4–1.8	0.25 ± 0.03	67.9
ZnO@ ZnS	8.7 ± 1.8 (C1) 27.9 ± 1.2 (B1)	49–57	1.4 ± 0.3	1.8–9.1	0.64 ± 0.04	0.3–1.9	0.22 ± 0.03	69.7
Ag-ZnO	8.2 ± 0.6	47–53	2.8 ± 0.5	0.5–5.3	0.8 ± 0.3	-	-	48.9
Ni-ZnO	1.5 ± 0.3	29–33	-	-	1.6 ± 0.2	0.3–2.9	0.54 ± 0.06	33.5

Table 1: Ratios of ZnS, Ag and Ni to ZnO, dimensions of central trunk and primary and secondary branches and the BET surface area of the fern-like ZnO-based microleaves.

Different textures of the fern-like microleaf surfaces were observed in the deposits, depending upon the synthesis process. However, the shape and architecture are not dramatically affected by the different synthesis procedures, except in the case of the Ni-doped branched-ZnO samples. The ZnO@ZnS core@shell structures (Figure 2b) presented slightly larger diameters of the central stipe and the ramifications, with a remarkable surface roughness when compared to as-electrodeposited ZnO fern-like microleaves. Note that the increase in diameter does not affect the architecture and, therefore, it should not deteriorate the access of the light or the pollutants to the structure. In fact, roughness can be very positive for photocatalysis, since the active area should be significantly increased. Importantly, the elemental maps of the ZnO@ZnS micro/nanofern fragments (**Figure S3a**) demonstrated the formation of ZnS

shell along the micro/nanofern. Due to the large size of the structures only the smaller secondary ramification can be reliably analyzed by EDX mapping due to excessive absorption and shadowing effects. Thus, it is not possible to obtain an average ZnS for the different parts of the structure, although in the studied parts a shell thickness in the range of 100 nm can be inferred. As can be seen in Figure 2c, the compactness increases dramatically when Ag is photodeposited on the ZnO fern-like structures. Ag is heterogeneously distributed along the ZnO surface but it is substantially more deposited on the central trunk, as the diameter is roughly doubled. The high photodeposition of Ag, especially along the central trunk, evidences the easy access for both reactant and light throughout the entire surface of micro/nanoferns. However, the elemental maps of Ag-decorated micro/nanoferns (**Figure S3b**) revealed the formation of a continuous layer of Ag along the ZnO surface, as well as the formation of nanoparticles on some ramifications, possibly as a consequence of the different surface reactivity and arrival of light during the photodeposition. Likewise, in the case of the co-deposition of Ni(II), the formation of more compact structures has been observed (Figure 2d), wherein the lateral growth of the primary (B1 in Figure 1) and secondary ramification (B2 in Figure 1) are multiplied by 3 and 2, respectively, and the longitudinal growth of central stipe (C1 in Figure 1) is limited (with lengths around 53% lower). This indicates that the bath composition is also extremely important to promote the growth of fern-like microleaves. In addition, the surface morphology of the Ni-doped ZnO presented a slightly higher roughness as compared to non-doped structures. In addition, the BET surface area measurements (Table 1) were consistent with the observed architectures and morphologies of each photocatalyst (**Figure S4**). The unmodified ZnO (67.9 $m^2 g^{-1}$) and ZnO@ZnS (69.7 $m^2 g^{-1}$) architectures offered a superior specific area to the Ag-decorated (48.9 $m^2 g^{-1}$) and Ni-doped (33.5 $m^2 g^{-1}$) ZnO micro/nanoferns due to the better dendritic definition of microleaves and reduced compactness. In spite of this, all the biomimetic-obtained photocatalysts revealed a higher specific area than most of the micro/nanometric ZnO-based photocatalysts, which was crucial to enhance photoremediation efficiency [22-30]. Therefore, fern-like ZnO-based photocatalysts may emerge as a more interesting architecture than simple microrods, nanorods or nanowires due to the (i) higher electron diffusion length; (ii) higher accessible specific surface area for pollutants and light; and (iii) higher capability to absorb light since this architecture due to

enhanced light trapping in the fractal architecture and trapping efficiency on the angle of the incident light (in contrast to what has been observed for other morphologies) [22, 23, 43, 56, 57].

Figure 3 shows the XRD patterns of the ZnO, ZnO@ZnS core@shell, Ag-decorated ZnO and Ni-doped ZnO fern-like bioinspired microleaves. All the photocatalysts presented a hexagonal wurtzite polycrystalline structure. As the results show, the principal diffraction peaks appear at $2\theta = 31.79^{o}$ (100), 34.42^{o} (002), 36.25^{o}(101),47.55^{o}(102), 56.60^{o}(110), 62.86^{o}(103), 66.35^{o}(200), and 67.96^{o}(112), in agreement with the standard wurtzite ZnO structure (JCPDS card No. 36-1451). Other three diffraction peaks at $2\theta = 26.6^{o}$(110), 51.7^{o}(211) and 61.2^{o} (310) are also detected, which correspond to SnO_2 (JCPDS card No. 46-1088) from fluorine-doped tin oxide substrates. Importantly, no peaks arising from impurities, such as $Zn(OH)_2$, were detected. Note that the strong diffraction (002) peak at $2\theta = 34.4^{o}$, especially for ZnO micro/nanoferns, prove the preferred orientation of the structures along the c-axis. The XRD of the ZnO@ZnS core@shell structures (curve ii in Figure 3) shows an important reduction in the intensity of the ZnO peaks because of the formation of an outer ZnS shell. In addition, two diffraction peaks appearing at $2\theta = 28.55^{o}$ (111) and 33.87^{o} (200) match perfectly with the cubic ZnS blende structure (JCPDS card No. 65-1691). The obtained results confirmed the formation of a ZnS shell over the ZnO surface. The FT-IR spectra (see Supporting Information) of the ZnO@ZnS core@shell are consistent with these results.

For the Ag-decorated-ZnO micro/nanoferns, the intensity of the ZnO peaks is also reduced because of the photodeposition of Ag on the ZnO surface (curve iii in Figure 3). The XRD pattern of Ag-decorated micro/nanoferns showed three extra peaks at $2\theta = 38.11^{o}$ (111), 44.27^{o} (200), and 64.42^{o} (311), which are in accordance to the face-centered cubic (*fcc*) Ag standard (JCPDS card No. 04-0783). The absence of any impurity peaks clearly demonstrated the high purity of as-prepared Ag-decorated ZnO photocatalysts. Finally, it is worth emphasizing that in the XRD pattern of Ni-doped ZnO bioinspired microleaves (curve iv in Figure 3) only ZnO wurtzite peaks were observed (i.e., with no precipitation of Ni phases), indicating that all the Ni incorporates in the ZnO structure.

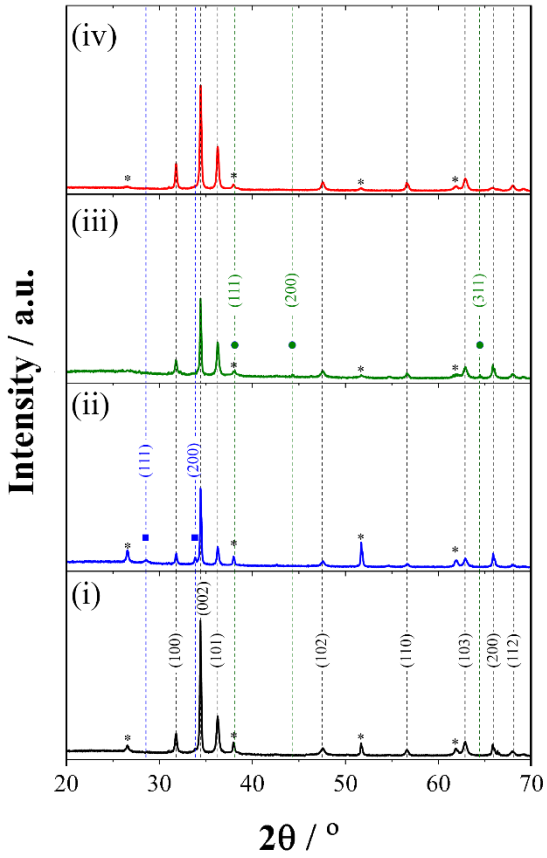

Figure 3: XRD patterns of (i) ZnO, (ii) ZnO@ZnS core@shell, (iii) Ag-decorated ZnO, and (iv) Ni-doped ZnO bioinspired fern-shape microleaves. The diffraction peaks that correspond to the cubic ZnS blende, face-centered cubic Ag, and fluorine-doped tin oxide substrate structures are indicated with ■, ●, and *.

The chemical state of Zn, Ag, and Ni in the fern-like bioinspired microleaves were investigated in detail by analyzing the Zn 2p, O 1s, S 2p, Ag 3d, and Ni 2p XPS spectra (**Figure 4**). The binding energies obtained from the XPS analysis were corrected for specimen charging by referencing the C 1s to 284.60 eV. From Figure 4a, it can be seen that the peaks of Zn $2p_{1/2}$ and Zn $2p_{3/2}$ core levels are centered at 1021.1 and 1044.3 eV. Ag-decorated and Ni-doped ZnO also have two peaks slightly shifted towards higher energy bindings due to differences in the morphologies. These values are similar to the ones reported for ZnO nanostructures, especially with ZnO nanowires [58-60]. Figure 4b shows the XPS

spectra of the O 1s region, which shows two different forms of oxygen. For ZnO and Ag-decorated ZnO, a quasi-symmetric peak centered at 530.1 eV is observed, which indicates the formation of ZnO. However, small peaks centered at 531.1 eV could be identified for these photocatalysts, which can be associated with oxygen vacancies. The two peaks are also observed for Ni-doped ZnO, but with a different relationship since the peak corresponding to the oxygen vacancies is higher. In the case of ZnO@ZnS micro/nanoferns, the two different peaks centered at 531.1 and 532.3 eV are associated with the oxygen vacancies and chemical adsorbed oxygen on the photocatalyst surface. Note that the lattice oxygen peak at 530.1 eV is suppressed due to the formation of a ZnS shell [58-60]. In addition, the S 2p XPS spectrum of the core@shell photocatalysts exhibits an asymmetric shape, with contributions of the S $2p_{1/2}$ and S $2p_{3/2}$ peaks centered at 162.8 and 161.5 eV, respectively, which demonstrates the formation of a ZnS shell [23]. In Figure 4d, two peaks located at 368.0 and 373.9 eV are observed for the Ag-decorated photocatalysts, which are assigned to Ag $3d_{5/2}$ and Ag $3d_{3/2}$ of Ag, respectively. Note that these results align with those obtained in the diffraction pattern, in which *fcc* Ag was detected [25]. Figure 4e shows the Ni 2p XPS spectra of the Ni-doped ZnO, in which the two peaks of Ni $2p_{1/2}$ and Ni $2p_{3/2}$ core levels are centered at 873.4 and 855.8 eV, respectively, whereas the corresponding satellite structures are clearly observed at 878.8 and 861.6 eV. These values show the absence of metallic Ni, since the obtained difference between Ni $2p_{1/2}$ and Ni $2p_{3/2}$ (17.6 eV) is very different from the value of metallic Ni (17.27 eV), and it is closer to the NiO value (17.49 eV). Therefore, this indicates that nickel is in the +2 oxidation state. According to the data, it seems plausible that the Ni(II) ions have been successfully incorporated in ZnO wurtzite structure, as suggested by the XRD results [61-63].

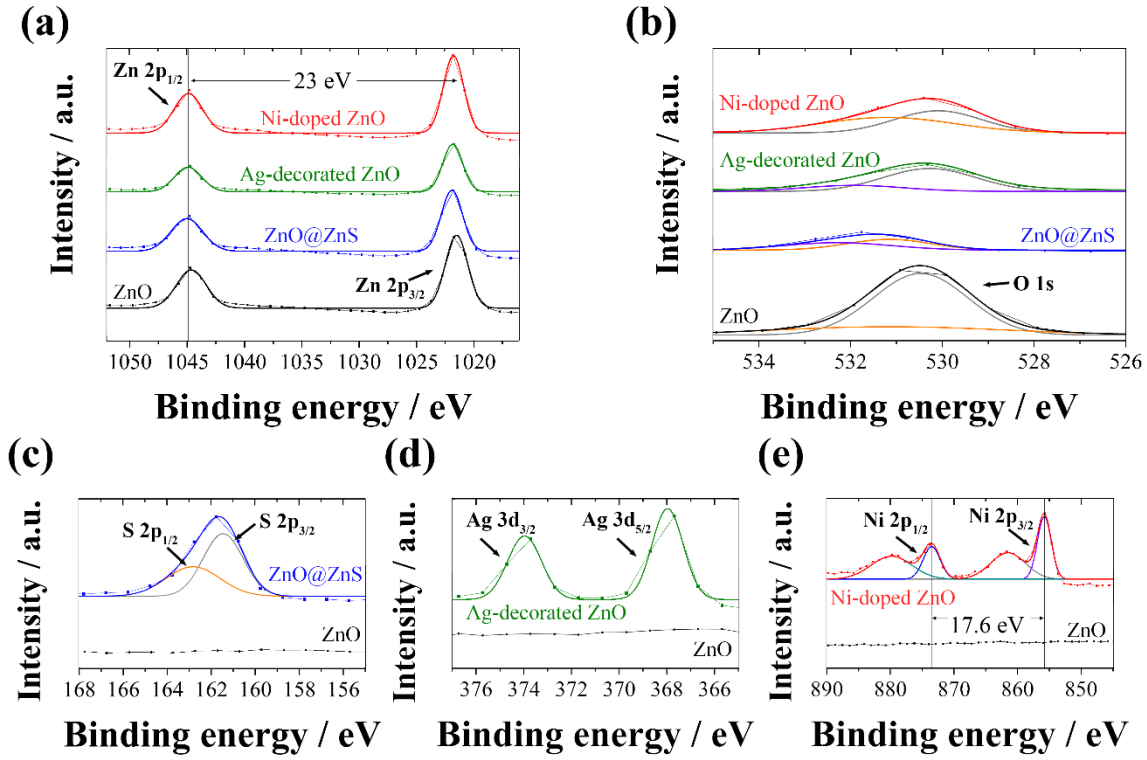

Figure 4: XPS spectra of (a) Zn 2p, (b) O 1s, (c) S 2p, (d) Ag 3d, and (e) Ni 2p of the ZnO, ZnO@ZnS core@shell, Ag-decorated ZnO, and Ni-doped ZnO bioinspired fern-shape microleaves.

The UV-visible DRS spectra of the ZnO, ZnO@ZnS core@shell, Ag-decorated ZnO, and Ni-doped ZnO bioinspired fern-shape microleaves are shown in **Figure 5a**. As expected, the absorbance spectra of the ZnO photocatalyst shows a strong absorption in the UV region and very small absorption intensity in the visible domain. However, when fern-like ZnO structures were modified by Ni-doping, Ag-decoration or a ZnS shell, the absorption band was displaced to the visible region. In addition, a clear absorption tail (with a notable absorption intensity) was observed in this region, indicating that these materials should present photoresponse in the visible range. Moreover, the optical band gaps of the samples were calculated using the Tauc relation (**Figure S5**) [64, 65]. The band gap of the ZnO, ZnO@ZnS core@shell, Ag-decorated ZnO, and Ni-doped ZnO bioinspired fern-shape microleaves was 3.29 ± 0.06, 2.73 ± 0.06, 3.00 ± 0.04, and 2.82 ± 0.05 eV, respectively, in agreement with literature data. The bandgap reduction also points towards an enhanced photoresponse in the visible range.

The change in the opto-electronic properties induced by the ZnO modification was also characterized by photoluminescence in the visible and near infrared (NIR) range. The unmodified ZnO structures showed a room temperature broad photoluminescence band centered around 650 nm. This band is redshifted with respect to other ZnO nanostructures [23] (whose maximum luminescence is usually centered at 550 nm), which is attributed to oxygen vacancy defects. Our growth conditions under high oxygen concentration and magnetic stirring probably minimize the oxygen vacancies during the growth, thereby leading to a broader and more redshifted luminescence linked to surface defects. Interestingly, a large two-fold rise of the photoluminescence intensity was observed for the ZnO@ZnS core@shell structures. Such enhancement in the visible-NIR spectral range is also an indicator of the band gap reduction at the ZnO/ZnS interface as a result of the large (16%) lattice mismatch between ZnO and ZnS [66]. The band gap reduction, together with the type II staggered heterojunction, which promote the separation of the photogenerated electrons and holes towards the ZnO and ZnS regions, respectively, are crucial to modify the photocatalytic pathway and to enhance the photocatalysis efficiency with visible-NIR light, as we will demonstrate below.

In contrast, a substantial reduction of the photoluminescence is observed in the Ag decorated ZnO sample, which can be mainly attributed to the quenching and large absorption of the emitted photons by the thick deposited Ag layer on the ZnO. Finally, the Ni-doped sample showed minimal changes with respect the unmodified ZnO structure, which again suggests that Ni is completely incorporated in the lattice and does not substantially increase the number of defects and trapped electronic states within the bandgap.

Photocurrent response measurements were explored in several on–off cycles of artificial UV-filtered sunlight irradiation to confirm both the photoexcited electron–hole pair generation and the separation in each photocatalyst. As shown in **Figure 5c**, the photocurrent of ZnO@ZnS (120 μA cm^{-2}), Ag-decorated (89 μA cm^{-2}), and Ni-doped ZnO (72 μA cm^{-2}) biomimetic photocatalysts showed relevant 2.8, 2.1, and 1.7 fold enhancements with respect to ZnO (43 μA cm^{-2}) micro/nanoferns, respectively, thereby suggesting that the different ZnO-modifications can improve the photocatalytic efficiency. In addition, the sharper photoswitching response of the Ag-decorated and particularly of the ZnO@ZnS heterojunction

architectures indicate not only that photoinduced electrons and holes can be easily separated, but also that the recombination process was hindered.

In addition, it is worth noting that the biomimetic fractal ZnO architectures exhibited 2-fold higher photocurrent than aligned non-branched ZnO nanowires (grown in the same conditions as the ZnO micro/nano ferns, but with low agitation). This suggests that the hierarchical structured enables a substantial improvement of the light trapping efficiency, as it is illustrated in **Figure 5d**. Remarkably, ZnO and ZnO@ZnS micro/nanoferns presented the same photoresponse when the photocatalysts were irradiated at different light incident angles (**Figure S7**), unlike the ZnO non-branched nanowires, which showed a 1.6-fold decrease at irradiation angles of 30° and 150°. In concordance with their low BET surface area, such independence on the angle of incidence of the light, worsened for the Ag-decorated and Ni-doped micro/nanoferns due to their higher compactness and reduced dendritical architectures. Therefore, these results highlight the great potential of the modified ZnO-based micro/nanoferns for efficient sunlight photocatalysis applications.

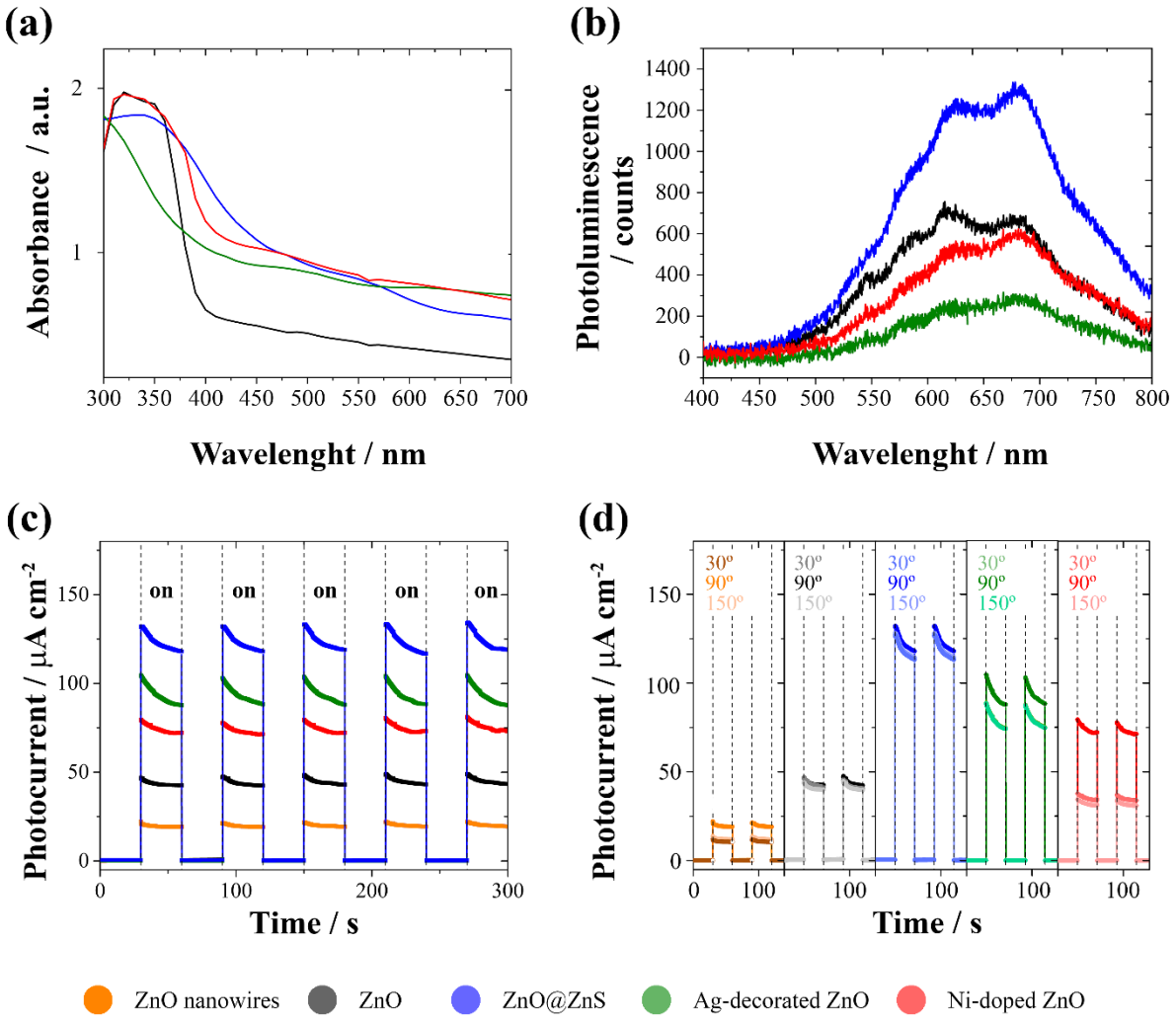

Figure 5: (a) UV-visible DRS absorption spectra, and (b) room temperature PL spectra of the ZnO, ZnO@ZnS core@shell, Ag-decorated ZnO, and Ni-doped ZnO bioinspired fern-shape microleaves. (c) Amperometric photocurrent curves of ZnO-based photocatalysts measured at 0.1 V versus Ag/AgCl/ KCl (3M) under visible light 30-s on–off cycles. (d) Photocurrent curves of ZnO-based photocatalyst as a function of light incidence irradiation angles (30°, 90°, and 150°) relative to the substrate.

3.1. Photocatalytic activity

The photodegradation efficiency of three different persistent organic pollutants (MB, 4-NP, and Rh-B) was studied under UV, artificial and natural UV-filtered sunlight irradiation in order to evaluate which bioinspired modified ZnO photocatalyst architecture presents a greater solar photocatalytic activity. Note that in the absence of photocatalysts, the pollutant concentration remains virtually constant (**Figure**

S8), regardless of the irradiation conditions, indicating that in these conditions pollutant photolysis can be neglected. The UV-visible absorption spectra of the pollutant alkaline solutions in the presence of photocatalysts at different irradiation times were used to estimate the degradation of each pollutant. As can be seen in **Figures 6** (MB), **S9** (4-NP) and **S10** (Rh-B), the absorption intensity of the different curves in the UV-Vis domain tends to decrease with the irradiation time until the absorption bands are no longer observed, which occurs at different times depending on the photocatalytic activity of each photocatalyst. Moreover, the photomineralization of each pollutant was evaluated by measuring the TOC content after the tests. As can be seen in **Tables 2** (degradation efficiency) and **3** (TOC reduction), the ZnO@ZnS core@shell bioinspired fern-shape microleaves photocatalyst presents the greatest degradation and mineralization efficiency, which is particularly relevant when UV-filtered sunlight is used as the irradiation source. Remarkably, the degradation efficiencies (**Figures 7a** (MB), **S12a** (4-NP), and **S13a** (Rh-B)**)**, under artificial UV-filtered light irradiation for the ZnO@ZnS core@shell, Ag-decorated ZnO, and Ni-doped ZnO bioinspired fern-shape microleaves were determined to be ~99%, ~90%, and ~90%, respectively. These values are significantly larger than those determined for non-modified ZnO biomimetic ferns (which ranged from 45 to 59% depending on the pollutant solution) (Table 2). In addition, the TOC reduction (**Figures 7c** (MB), **S12c** (4-NP), and **S13c** (Rh-B)) for the modified ZnO structures is significantly higher than that obtained with pristine ZnO photocatalysts. Note that the TOC reduction (Table 3), which indicates the total mineralization of pollutants, is very similar to the photodegradation efficiency obtained from the UV-vis spectra in the different irradiation conditions, especially for the photodegradation of MB.

Photocatalyst	Pollutant	Degradation efficiency under UV in 120 min (λ= 365 nm)	Degradation efficiency under artificial UV-filtered sunlight in 120 min (λ> 400 nm)	Degradation efficiency under UV-filtered solar sunlight in 120 min (λ> 400 nm)	Mass normalized kinetic constant under UV (λ= 365 nm) / min^{-1} g^{-1}	Mass normalized kinetic constant under artificial UV-filtered sunlight (λ> 400 nm)/ min^{-1} g^{-1}	Mass normalized kinetic constant under UV-filtered sunlight (λ> 400\ nm)/ min^{-1} g^{-1}
ZnO	**MB**	80 ± 2%	59 ± 1%	45 ± 2%	3.38	1.85	1.23
	4-NP	83 ± 2%	45 ± 2%	30 ± 3%	3.75	1.24	0.75
	Rh-B	88 ± 1%	56 ± 2%	34 ± 3%	4.28	1.71	0.84
ZnO@ZnS	**MB**	95 ± 1%	99 ± 1%	98 ± 2%	5.98	8.28	7.53
	4-NP	92 ± 2%	98 ± 1%	97 ± 1%	5.07	8.21	7.41
	Rh-B	88 ± 1%	98 ± 1%	96 ± 1%	4.31	7.30	6.75
Ag-ZnO	**MB**	83 ± 1%	93 ± 2%	84 ± 2%	3.63	5.38	3.73
	4-NP	84 ± 2%	90 ± 1%	85 ± 1%	3.78	5.20	3.57
	Rh-B	84 ± 1%	87 ± 1%	83 ± 1%	3.80	3.99	3.78
Ni-ZnO	**MB**	87 ± 2%	91 ±1%	84 ± 3%	4.38	4.95	3.62
	4-NP	86 ± 1%	89 ± 2%	83 ± 1%	4.05	4.39	3.74
	Rh-B	83 ± 1%	92 ± 2%	77 ± 2%	3.49	5.08	3.13

Table 2: Photocatalytic degradation efficiency of MB (10 ppm), 4-NP (10 ppm), and Rh-B (5 ppm) polluted solutions under UV light (λ = 365 nm), artificial UV-filtered sunlight (λ> 400 nm) and natural UV-filtered sunlight (λ> 400 nm) using (0.4 mg mL^{-1}) the ZnO, ZnO@ZnS core@shell, Ag-decorated ZnO, and Ni-doped ZnO bioinspired fern-shape microleaves.

Moreover, the mass-normalized kinetic constant (k_{nor}) of each photocatalyst for all the irradiation conditions was determined in order to examine the kinetics of degradation and to compare all the mass-normalized kinetic constants to the state-of-the-art MB, 4-NP, and Rh-B ZnO-based photocatalysts. According to the Langmuir-Hinshelwood model, the photocatalytic degradation can be considered to follow a pseudo-first-order kinetics with respect to the pollutant concentrations at low concentrations. The logarithmic plot of the absorbance ($-\ln(A_t/A_0)$) as a function of the reaction time (t) (**Figure S11**) allows the calculation of the apparent kinetic constant (k_{app}) in accordance with the following equation (Eq. 1):

$$\left(\frac{dc}{dt}\right) = -k_{app}c_t \rightarrow ln\left(\frac{c_t}{c_0}\right) = ln\left(\frac{A_t}{A_0}\right) = -k_{app}t$$

where c_t is the pollutant concentration that remains in the solution after irradiation time (t), A_t is the maximum absorbance of each pollutant after irradiation time (t), c_0 is the initial pollutant concentration, and A_0 is the initial absorbance of the peak. Note that the apparent kinetic constant depends on the photocatalyst surface, nature, active sites, electronic properties, and light trapping efficiency. The normalized kinetics constant ($k_{nor} = k_{app}/m_{catalyst}$) allows the comparisons between the photocatalytic activity of each photocatalyst (**Table 2**).

Photocatalyst	Pollutant	TOC of pollutant solution without irradiation	TOC reduction after 120 min under UV (λ= 365 nm)	TOC reduction after 120 min under artificial UV-filtered sunlight (λ> 402 nm)	TOC reduction after 120 min under UV-filtered solar sunlight (λ> 402 nm)
ZnO	MB	9.87 ± 0.05	77.5 ± 1.1%	54.1 ± 0.9%	43.2 ± 1.6%
	4-NP	9.86 ± 0.04	79.3 ± 1.4%	44.2 ± 1.0%	28.8 ± 0.9%
	Rh-B	4.96 ± 0.22	82.3 ± 1.3%	47.4 ± 1.2%	31.2 ± 1.1%
ZnO@ZnS	MB	10.05 ± 0.13	94.5 ± 1.6%	99.1 ± 1.2%	98.2 ± 1.9%
	4-NP	10.34 ± 0.05	88.4 ± 1.1%	98.2 ± 1.5%	97.8 ± 1.8%
	Rh-B	4.48 ± 0.12	86.2 ± 1.4%	97.1 ± 1.4%	95.8 ± 1.8%
Ag-ZnO	MB	11.45 ± 0.13	82.1 ± 1.2%	90.6 ± 2.4%	81.7 ± 1.5%
	4-NP	10.71 ± 0.09	79.3 ± 0.9%	84.7 ± 1.1%	82.4 ± 1.4%
	Rh-B	5.39 ± 0.08	81.3 ± 1.2%	85.2 ± 2.2%	81.1 ± 0.7%
Ni-ZnO	MB	11.45 ± 0.13	84.5 ± 1.1%	88.0 ± 1.0%	82.1 ± 1.6%
	4-NP	10.75 ± 0.12	85.3 ± 2.1%	84.1 ± 1.0%	81.0 ± 2.1%
	Rh-B	5.48 ± 0.05	80.5 ± 1.6%	87.8 ± 0.8%	78.1 ± 0.4%

Table 3: Photocatalytic degradation efficiency of MB (10 ppm), 4-NP (10 ppm), and Rh-B (5 ppm) polluted solutions under UV light (λ = 365 nm), artificial UV-filtered light (λ> 400 nm) and natural UV-

filtered sunlight (λ> 400 nm) using (0.4 mg mL^{-1}) ZnO, ZnO@ZnS core@shell, Ag-decorated ZnO, and Ni-doped ZnO bioinspired fern-shape microleaves.

As can be seen in **Figures 7b** (MB), **S12b** (4-NP) and **S13b** (Rh-B), under UV-filtered sunlight irradiation, the pollutant degradation rate of the ZnO@ZnS core@shell architecture is about 6.1 (MB), 9.9 (4-NP), and 8.0 (Rh-B) times higher than that of the unmodified ZnO micro/nanoferns, and about twice higher than that of Ag-decorated ZnO micro/nanoferns, and the Ni-doped micro/nanoferns for the three pollutants. Interestingly, similar photodegradation rates were obtained in the three irradiation conditions for the Ag-decorated ZnO and the Ni-doped ZnO bioinspired micro/nanoferns, despite the difference in band-gap energy. This implies that the change in band-gap is compensated by the higher surface area (and thus easy pollutant and light accessibility) of the Ag-decorated ZnO micro/nanoferns. Moreover, it is worth emphasizing that the k_{nor} of ZnO@ZnS core@shell bioinspired micro/nanoferns, listed in Table 2, are similar or even higher than that of the most competitive state-of-the-art ZnO-based photocatalysts (**Tables S1-S3**) [23, 29, 34, 67-86]. Therefore, in relation to the photocatalytic activity, the ZnO@ZnS core@shell bioinspired fern-shape microleaves exhibit an outstanding photocatalyzed remediation for the three different studied pollutants with a catalytic performance rivaling with doped ZnO nano-catalysts. In this regard, the visible photocatalytic pollutant degradation performance of the ZnO@ZnS core@shell micro-fern architecture is significantly higher than that obtained with the vertically aligned ZnO@ZnS core@shell nanorods [23]. This clearly highlights the improvement of the bioinspired architecture in terms of the light trapping and pollutant accessibility, resulting in enhanced photocatalytic performance.

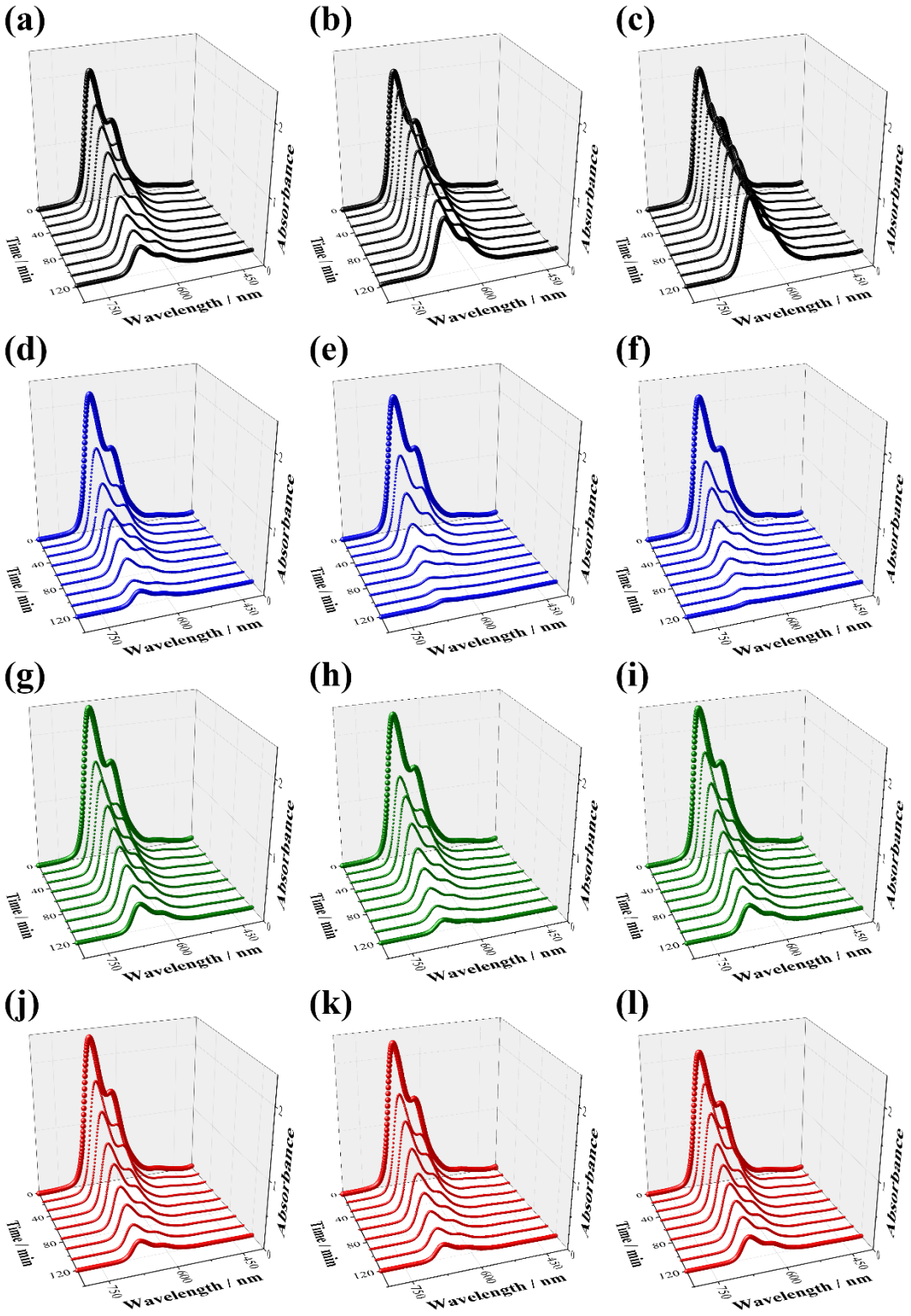

Figure 6: Time-dependent UV–vis spectra of the MB photocatalyzed degradation under (a, d, g, and j) UV light (λ = 365 nm), (b, e, h, and k) artificial UV-filtered sunlight (λ> 400 nm), and (c, f, i, and l)

UV-filtered sunlight (λ> 400 nm) using 0.4 mg mL^{-1} of (a-c) ZnO, (d-f) to the ZnO@ZnS core@shell, (g-i) to the Ag-decorated ZnO, and (j-l) to the Ni-doped ZnO bioinspired fern-shape microleaves.

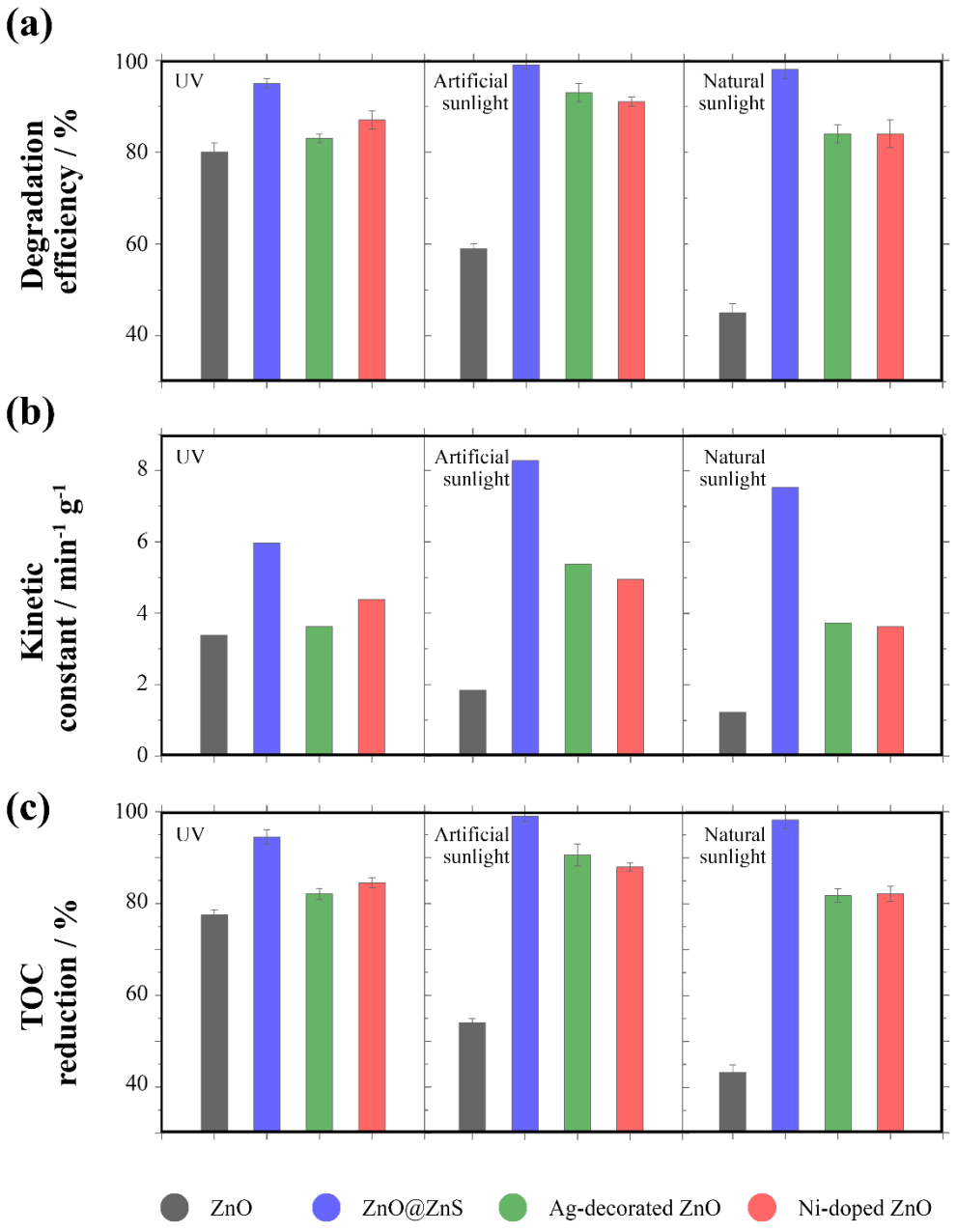

Figure 7: Comparison of (a) degradation efficiency; (b) the mass-normalized kinetic constant; and (c) percentage of the total organic carbon reduction during the irradiation of MB polluted solution under UV light (λ = 365 nm), artificial UV-filtered sunlight (λ> 400 nm) and natural UV-filtered sunlight (λ> 400 nm) using 0.4 mg mL^{-1} of ZnO, ZnO@ZnS core@shell, Ag-decorated ZnO, and Ni-doped ZnO bioinspired fern-shape microleaves.

3.2. Photocorrosion resistance

Since ZnO is renowned for its high instability under illumination, we evaluated the photocorrosion resistance for different photocatalysts. The successive pollutant degradation efficiencies, after the continuous irradiation of the photocatalysts in the pollutant solution (MB, 4-NP, or Rh-B) and fresh water for 0 to 48 h under artificial UV-filtered sunlight, were used to evaluate the photostability, photocorrosion, and recyclability of ZnO-based microleaves (**Figures 8a, S14**). For all the photocatalysts in up to three cycles (after 15 h of irradiation in the pollutant solution and fresh water), no significant reduction in the degradation efficiencies was observed. However, the ZnO and Ni-doped ZnO structures presented the lowest photostability since photocatalytic activity is significantly reduced in successive reaction cycles after 15 h of irradiation. The photodegradation efficiency after five cycles (48 h of total irradiation time) is approximately 18-21% for ZnO and 49- 54% for Ni-doped ZnO photocatalysts. Despite the significant reduction for both photocatalysts, Ni-doped ZnO presented greater reusability capability as the relative reduction of the photodegradation efficiency was approximately 41-44%, while the non-modified architecture presented a reduction as high as 63-70%. Notably, the photodegradation efficiency for the Ni-doped ZnO slightly improved in the first cycles, possibly because of the Zn(II) dissolution during this 15 h of irradiation, which resulted in an increase of the surface area, and consequently, better pollutant and light accessibility. Conversely, the Ag-decorated ZnO and, more remarkably, the ZnO@ZnS core@shell microleaves presented a significantly stable photocatalytic activity, even after recycling five times and irradiating for 48 h. In particular, the photodegradation efficiency for the ZnO@ZnS core@shell architectures remained virtually constant even after 48 h. Therefore, the reduction in photodegradation efficiency after 48 h of continuous irradiation and 5 consecutive cycles demonstrated that photocatalyst nature has a determining effect on photocatalytic activity, as ZnO@ZnS core@shell architectures only presented a reduction of approximately 2-4%. These values are approximately 22, 17, and 3 times lower than those obtained for ZnO, Ni-doped ZnO, and Ag-decorated ZnO micro/nanoferns, respectively. In addition, the concentration of Zn(II) ions in fresh water was determined after the continuous irradiation of photocatalysts during 0, 3, 6, 15, 30, and 48 h under UV (λ= 365 nm) and artificial UV-filtered sunlight (λ> 400 nm) to evaluate the photostability of each photocatalyst. The concentration

of Zn(II) in solution was also determined for each photocatalyst after 48 h of immersion in fresh water in dark conditions (**Figure S14a**) and under irradiation. The amount of dissolved photocatalyst after 48 h of immersion in fresh water clearly depends on the catalyst's chemical nature as well as the irradiation conditions, since the concentration of Zn(II) in solution was less than 5 μM for all the photocatalysts in dark conditions, while it was as high as 3.6 mM for the unmodified architecture when irradiated with UV light (**Figure S14b**). The relative release of Zn(II) in solution in relation to the initial amount of catalysts after 48 h of artificial UV-filtered sunlight was approximately 45%, 2.2%, 9.7%, and 44% for ZnO, ZnO@ZnS core@shell, Ag-decorated ZnO, and Ni-doped ZnO bioinspired fern-shape micro-leaves, respectively. A similar tendency, but with a slightly higher Zn(II) dissolution, were observed when the photocatalysts were irradiated with UV light (**Figure S15b**). Note that the core@shell architectures presented a practically identical minimal dissolution of Zn in both UV and artificial UV-filtered light, which confirmed its superior photocorrosion resistance. Initially, the dissolution of Zn increased the accessible surface area, and consequently the photodegradation efficiency, as observed during the first cycles of Ni-doped photocatalyst. However, the Zn(II) dissolution finally translated into an important reduction of the photocatalytic activity and the reusability, as the amount of catalyst and its area decreased. The XRD pattern of each reused photocatalyst (**Figure S16**) shows that neither the mineralization of the pollutants nor the irradiation conditions affect the crystalline structure of each photocatalyst. However, the intensity of the peaks of the FTO substrate is slightly higher for the different catalysts, except for ZnO@ZnS core@shell micro/nanoferns. This is the consequence of the dissolution of the ZnO, which increases the exposure of the substrate. **Figure S17** shows the surface morphology of each photocatalyst after 3 and 48 h of irradiation. The high photocorrosion rate for the unmodified micro/nanoferns induced a clear deterioration of catalyst surface, already after 3 h of irradiation, which was more relevant and accompanied by the detachment of catalyst fragments after 48 h of continuous irradiation (**Figure S17a-c**). Importantly, no appreciable changes were observed in neither the architecture nor surface morphology of the ZnO@ZnS core@shell micro/nanoferns (**Figure S17d-f**). The Ag-decorated ZnO photocatalyst also exhibited an excellent photocorrosion resistance that was confirmed by the analysis of the surface during the irradiation process as most of the surface was practically unaltered, except some affected local regions that were thinned because of the high Zn dissolution due to the

low content of Ag (**Figure S17g -i**). Lastly, an important increase in the surface roughness of Ni-doped photocatalyst was observed, which justifies the initial increase in the photodegradation efficiency, followed by an important dissolution that reduced the amount of catalyst by the reduction of the width of the different ramifications (**Figure S17j -l**). Therefore, ZnO and Ni-doped ZnO have an important limitation for their practical use in photocatalysis, since it is imperative in terms of real and environmentally friendly applications for heterogeneous catalysts to be stable and reusable. Note that the adsorption and remediation of the different pollutants and intermediates had no effect on the photostability of the catalysts, ruling out any poisoning of the catalyzer. The non-poisoning of the photocatalyst was clearly demonstrated when comparing the values of the reduction in photodegradation efficiency and the percentage of dissolved Zn in relation to the initial amount of photocatalyst, especially for ZnO@ZnS core@shell, Ag-decorated ZnO, and Ni-doped ZnO. In addition, the excellent photostability, low photocorrosion activity, and low catalyst poisoning of the Ag-decorated ZnO and the ZnO@ZnS core@shell microleaves, greatly facilitate their recyclability and, hence, enhance their potential as photocatalysts for water remediation.

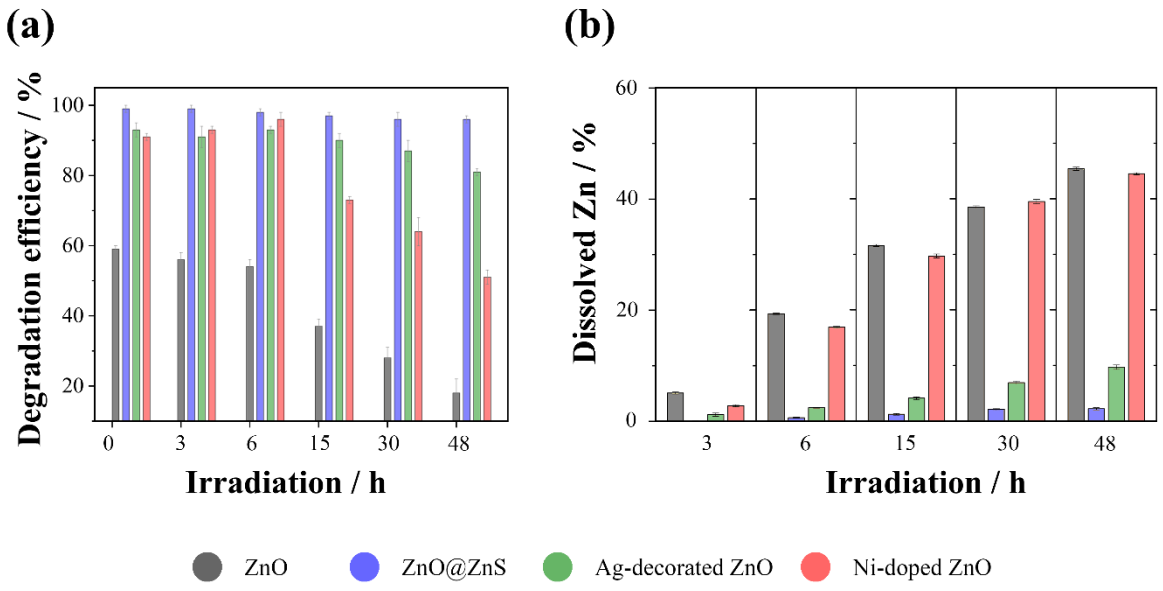

Figure 8: (a) Photocatalyst reusability of the ZnO, ZnO@ZnS core@shell, Ag-decorated ZnO, and Ni-doped ZnO bioinspired fern-shape microleaves (0.4 mg mL^{-1}) in cyclic photodegradation experiments (120 min) of MB for five consecutive cycles after the continuous irradiation of photocatalyst in MB

solution or fresh water during 0, 3, 6, 15, 30, and 48 h under artificial UV-filtered sunlight (λ> 400 nm). (b) Percentage of dissolved Zn (relative to the initial amount of Zn in each ZnO-based photocatalyst) after the continuous irradiation of 0.4 mg mL^{-1} of photocatalyst in fresh water during 3, 6, 15, 30, and 48 h also under artificial UV-filtered sunlight (λ> 400 nm).

3.3. Photocatalytic mechanism

The mineralization of pollutants is possible due to the fact that the additional charge carriers (e^-/h^+) and reactive oxygen species, such as superoxide and hydroxyl radicals, are generated on the photocatalysts surface. It is well known that hydroxyl radicals are the main actors in the mineralization mechanism of persistent organic pollutants. It is also important to consider the formation of oxygen superoxide and singlet oxygen species. However, the different photocatalytic activity strongly depends on the kinetics of formation of each reactive oxygen species. The particularities of the photocatalysis and the formation of the reactive oxygen species of these four biomimetic photocatalysts were studied by different selective chemical reactions and trapping experiments during the photodegradation of MB by using different scavengers to consume the corresponding generated active species, which affects the photodegradation efficiency. All the experiments were performed under artificial UV-filtered sunlight (λ> 400 nm) irradiation.

Figure 9a,b shows the time-dependent evolution of the concentration of fluorescein sodium salt and the rate of hydroxyl radical formation calculated from the intensity of the photoluminescence peak at 515 nm (λ_{ex} = 303 nm) of the time-dependent photoluminescence spectra. Note that the kinetic rate was calculated by assuming zero order kinetics between hydroxyl radical and fluorescein sodium salt (**Figure S18**) [52]. The kinetics of hydroxyl formation in the absence of photocatalyst have also been considered, since the photolysis of water, which is especially relevant under UV irradiation, can also be an important source of hydroxyl radicals. However, under artificial UV-filtered sunlight, photolysis is practically negligible since the kinetics of hydroxyl radical formation is 7, 350, 154, and 139 times lower than that obtained when ZnO, ZnO@ZnS, Ag-decorated, and Ni-doped micro/nanoferns, receptively, are used. The order of hydroxyl radical output is ZnO@ZnS > Ag-decorated > Ni-doped > ZnO micro/nanoferns, which is exactly the same tendency observed for the photodegradation of MB, 4-NP, and

Rh-B pollutants. Therefore, the formation of hydroxyl radicals has a capital role in the photo-mineralization of organic pollutants. Note that hydroxyl radicals can be formed mainly by (i) the reaction of photogenerated holes and/or electrons with adsorbed water or hydroxyl ions; (ii) the reaction of superoxide radicals with protons; and (iii) the photolysis of water. Therefore, elucidating which is the main source of generation of hydroxyl radicals in the case of ZnO@ZnS can be key to understand the exceptional photocatalytic activity to mineralize organic pollutants.

As can be seen in **Figure 9c,** for the ZnO@ZnS micro/nanoferns the formation of superoxide radicals is practically insignificant compared to other photocatalysts. On the other hand, Ag-decorated ZnO micro/nanoferns exhibited extensive activity to generate superoxide radicals, although it is significantly lower for Ni-doped ZnO and ZnO micro/nanoferns. Superoxide radicals do not have a high capacity for the photo-mineralization of organic contaminants in aqueous solution due to their low oxidation power, especially when compared to hydroxyl radicals. Therefore, the main function in an aqueous solution (protic media) is the formation of hydroxyl radicals when reacting with protons. However, in alkaline media, this reaction is more limited. Note that for ZnO@ZnS micro/nanoferns their contribution in the formation of hydroxyl radicals is minimal. In addition, the formation of singlet oxygen was also evaluated by both measuring the consumption of the singlet oxygen sensor reagent (**Figure S19)** and the formation of the endoperoxide compound (**Figure 9c**). From the time-dependent spectra of the formation of singlet oxygen the following order of activity is found: ZnO > Ni-doped ZnO > Ag-decorated ZnO > ZnO@ZnS micro/nanoferns. According to these experiments and the mineralization efficiency, hydroxyl radicals are clearly the most important reactive oxygen species involved in the mineralization process of persistent organic pollutants under UV-filtered irradiation when ZnO-based photocatalysts are used.

Lastly, trapping experiments of the active species during the photocatalytic degradation of MB using the ZnO, ZnO@ZnS core@shell, Ag-decorated ZnO, and Ni-doped ZnO bioinspired fern-shape microleaves photocatalysts were performed to visualize the effect of hydroxyl radicals, superoxide radicals, and photogenerated holes on the photodegradation process (**Figure 9d**). The degradation efficiency of ZnO (~45%) decreased to ~10%, ~33%, and ~28% in the presence of superoxide radical, hydroxyl rad-

ical, and hole scavengers, respectively. The marked decrease when benzoquinone was added demonstrates that the dominant factor during the degradation process was the superoxide radicals, which are coherent due to their low capability to produce hydroxyl radicals (0.012 μM min^{-1}) and their high capability to generate superoxide radicals in these irradiating conditions. However, the MB photodegradation efficiency of the ZnO@ZnS photocatalyst (~99%) decreased to ~92%, ~9%, and ~6% in the presence of superoxide radical, hydroxyl radical, and hole quenchers, respectively. Therefore, the photogenerated holes and the hydroxyl radicals govern the photocatalytic degradation when the ZnO@ZnS core@shell micro/nanoferns are used as photocatalysts. Therefore, the exceptional photocatalytic activity of ZnO@ZnS core@shell micro/nanofern can be attributed the combined effects of the improved light trapping efficiency given by the fractal architecture, and the electronic modifications caused by the heterojunction that enables a complete modification of the photocatalytic pathway towards the photogeneration of hydroxyl radicals. Such pathway change is provided by the ZnO/ZnS interface, which induces a substantial reduction of the bandgap [23], and the correct separation of the electron-hole pairs. The different conduction and valence band energy levels and electronic affinities of ZnO and ZnS promote the separation of the electrons and holes towards the ZnO and ZnS, respectively. Such separation is crucial to trap the holes at the ZnS/water interface, where the hydroxyl radicals can be efficiently generated. This reduction process is also key to protect the Zn structure by minimizing the release of Zn(II) that is the responsible of the fast photodegradation of the unmodified ZnO.

For the Ag-decorated ZnO micro/nanoferns (~93%), the catalytic process is similar to the pristine ZnO, as the efficiency decreased to ~2%, ~31% and ~27% in the presence of superoxide radical, hydroxyl radical, and hole quenchers, respectively, which indicates that the superoxide radicals are the predominant species during photocatalysis. Lastly, for the Ni-doped ZnO micro/nanoferns, all the quenchers influenced the photodegradation efficiency; however, the photodegradation efficiency decreased slightly when the superoxide quencher was added.

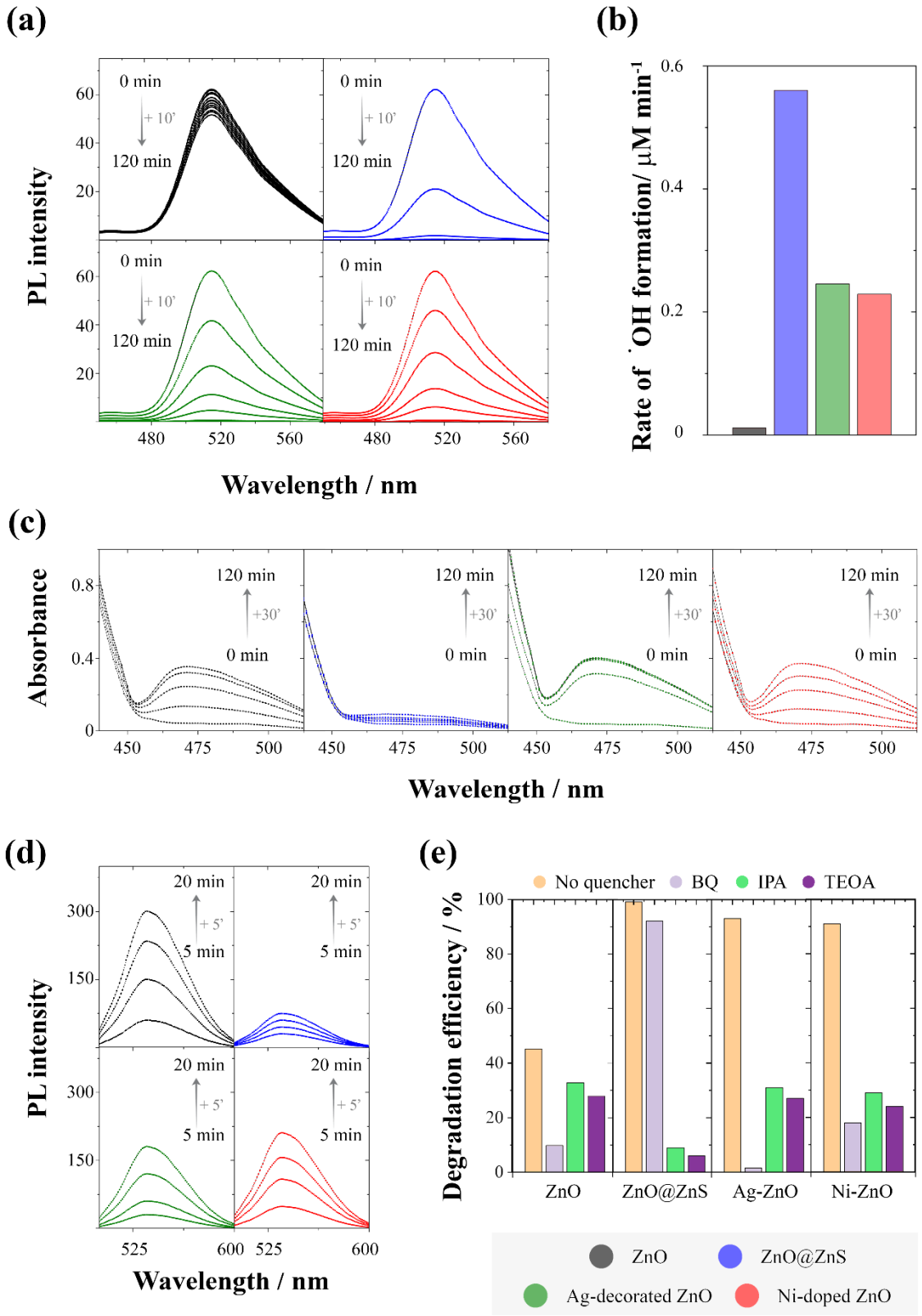

Figure 9: (a) Time-dependent photoluminescence spectra of 8 μM of the aqueous solution of fluorescein sodium (interval time between each measurement: 10 min), (b) rate of formation of hydroxyl radicals, (c) time-dependent UV-vis spectra of the formation of XTT-formazan indicating superoxide formation

(interval time between each measurement: 30 min), and (d) time-dependent photoluminescence spectra of endoperoxide formation indicating oxygen singlet formation (interval time between each measurement: 5 min) under artificial UV-filtered sunlight ($\lambda > 400$ nm) using 0.4 mg mL^{-1} of ZnO, ZnO@ZnS core@shell, Ag-decorated ZnO, and Ni-doped ZnO bioinspired fern-shape microleaves. (e) Trapping experiment of active species during the MB photodegradation under visible sunlight ($\lambda > 400$ nm) of the ZnO, ZnO@ZnS core@shell, Ag-decorated ZnO, and Ni-doped ZnO bioinspired fern-shape microleaves (0.4 mg mL^{-1}). BQ, IPA, and TEOA are used to indicate benzoquinone, isopropyl alcohol, and triethanolamine quenchers, respectively.

4. CONCLUSIONS

A new, simple, green, and inexpensive electrochemical synthesis pathway for the preparation of biomimetic ZnO and ZnO-based photocatalysts with fractal morphology has been established. Different modification processes, sulfidation-induced ZnS shell, Ag photodeposition, and Ni codeposition processes were used to modulate the photocatalytic activity of fractal ZnO micro/nanoferns, which allowed us to obtain competitive photocatalysts for the photodegradation and photoremediation of three different persistent organic pollutants, namely methylene blue, 4-nitrophenol, and Rhodamine B. The modified ZnO bioinspired photocatalysts have been shown to be excellent catalysts for the photodegradation and photo-remediation of contaminants by using UV light and artificial and natural UV-filtered sunlight. Both the photocatalyst architecture and the photocatalyst surface state played an important and synergetic rile in the photocatalytic performance, which is comparable to or better than the most competitive micro- and nano-metric state-of-the-art ZnO-based photocatalysts. The results highlight that the different modification processes and the biomimetic architecture of the doped ZnO bioinspired fern-like microleaves fixed on fluorine-doped tin oxide substrates (i) allow the modulation of the band gap to extend the photocatalytic activity to the visible domain and promote the separation of photogenerated electron-hole pairs and (ii) favor the absorption of light as it enhances their independence on the incident light angle. The ZnO@ZnS core@shell, Ag-decorated ZnO, and Ni-doped ZnO structures exhibited similar

– or even higher – photocatalytic activity compared to the benchmark ZnO-based photocatalysts, although Ni doping does not contribute to the chemical stability of the structure. Significantly, the ZnO@ZnS core@shell micro/nanoferns have demonstrated the best photocatalytic performance, promoted by their excellent opto-electronic properties, likely induced by the different crystallographic structure of the ZnO core and ZnS shell. The core@shell structures are highly competitive photocatalysts for practical applications not only because of their outstanding photocatalytic activity in the remediation of pollutants but also for their excellent recyclability and remarkably high photocorrosion resistance.

Acknowledgements

This work was partially supported by the Metrohm foundation. Partial funding from the 2017-SGR-292 project from the Generalitat de Catalunya, and the PCIN2016-093 and TEC2017-85059-C3-2-R projects (co-financed by the Fondo Europeo de Desarrollo Regional, FEDER) from the Spanish Ministerio de Economía y Competitividad (MINECO) is also acknowledged. ICN2 is funded by the CERCA Programme/Generalitat de Catalunya. ICN2 also acknowledges the support from the Severo Ochoa Program (MINECO, Grant No. SEV-2013-0295). Yue Zhang acknowledges the China Scholarship Council (CSC) for financial support (201608310112).

Appendix A. Supplementary data

Supplementary data related to this article can be found, in the online version, at doi:

References

[1] D. Mara, The all-inclusive sustainable development goals: the WASH professional's guide (or should that be 'nightmare?), J. Water Sanit. Hyg. Dev. 6 (2016) 349–352. doi:10.2166/washdev.2016.053.

[2] United Nations General Assembly 2015. The Human Rights to Safe Drinking Water and Sanitation (Document A/C.3./70/L.55/Rev.1, 17 December). United Nations, New York, NY.

[3] United Nations, Goal 6: Ensure availability and sustainable management of water and sanitation for all. https://unstats.un.org/sdgs/report/2017/goal-06/, 2018 (accessed 14 August 2018).

[4] M.A. Shannon, P.W. Bohn, M. Elimelech, J.G. Georgiadis, B.J. Marĩas, A.M. Mayes, Science and technology for water purification in the coming decades, Nature. 452 (2008) 301–310. doi:10.1038/nature06599.

[5] P. Devi, A.K. Saroha, Utilization of sludge based adsorbents for the removal of various pollutants: A review, Sci. Total Environ. 578 (2017) 16–33. doi:10.1016/j.scitotenv.2016.10.220.

[6] M. Concetta Tomei, A.J. Daugulis, Ex situ bioremediation of contaminated soils: An overview of conventional and innovative technologies, Crit. Rev. Environ. Sci. Technol. 43 (2013) 2107–2139. doi:10.1080/10643389.2012.672056.

[7] I. Oller, S. Malato, J.A. Sánchez-Pérez, Combination of Advanced Oxidation Processes and biological treatments for wastewater decontamination-A review, Sci. Total Environ. 409 (2011) 4141–4166. doi:10.1016/j.scitotenv.2010.08.061.

[8] E. Brillas, C.A. Martínez-Huitle, Decontamination of wastewaters containing synthetic organic dyes by electrochemical methods. An updated review, Appl. Catal. B Environ. 166–167 (2015) 603–643. doi:10.1016/j.apcatb.2014.11.016.

[9] J.M. Herrmann, C. Duchamp, M. Karkmaz, B.T. Hoai, H. Lachheb, E. Puzenat, C. Guillard, Environmental green chemistry as defined by photocatalysis, J. Hazard. Mater. 146 (2007) 624–629. doi:10.1016/j.jhazmat.2007.04.095.

[10] R. Andreozzi, V. et al Caprio, Advanced oxidation processes (AOP) for water purification and recovery, Catal. Today. 53 (1999) 51–59. doi:/10.1016/S0920-5861(99)00102-9.

[11] C. Santhosh, V. Velmurugan, G. Jacob, S.K. Jeong, A.N. Grace, A. Bhatnagar, Role of nanomaterials in water treatment applications: A review, Chem. Eng. J. 306 (2016) 1116–1137. doi:10.1016/j.cej.2016.08.053.

[12] O.F. Lopes, K.T.G. Carvalho, A.E. Nogueira, W. Avansi, C. Ribeiro, Controlled synthesis of BiVO4photocatalysts: Evidence of the role of heterojunctions in their catalytic performance driven by visible-light, Appl. Catal. B Environ. 188 (2016) 87–97. doi:10.1016/j.apcatb.2016.01.065.

[13] A. Serrà, S. Grau, C. Gimbert-Suriñach, J. Sort, J. Nogués, E. Vallés, Magnetically-actuated mesoporous nanowires for enhanced heterogeneous catalysis, Appl. Catal. B Environ. 217 (2017) 81–91. doi:10.1016/j.apcatb.2017.05.071.

[14] K. Kasinathan, J. Kennedy, M. Elayaperumal, M. Henini, M. Malik, Photodegradation of organic pollutants RhB dye using UV simulated sunlight on ceria based TiO2nanomaterials for antibacterial applications, Sci. Rep. 6 (2016) 38064. doi:10.1038/srep38064.

[15] M. Oelgemoller, Solar Photochemical Synthesis: From the Beginnings of Organic Photochemistry to the Solar Manufacturing of Commodity Chemicals, Chem. Rev. 116 (2016) 9664–9682. doi:10.1021/acs.chemrev.5b00720.

[16] J.H. Kim, H. Kaneko, T. Minegishi, J. Kubota, K. Domen, J.S. Lee, Overall Photoelectrochemical Water Splitting using Tandem Cell under Simulated Sunlight, ChemSusChem. 9 (2016) 61–66. doi:10.1002/cssc.201501401.

[17] R. Pol, M. Guerrero, E. García-Lecina, A. Altube, E. Rossinyol, S. Garroni, M.D. Baró, J. Pons, J. Sort, E. Pellicer, Ni-, Pt- and (Ni/Pt)-doped TiO_2 nanophotocatalysts: A smart approach for sustainable degradation of Rhodamine B dye, Appl. Catal. B Environ. 181 (2016) 270–278. doi:10.1016/j.apcatb.2015.08.006.

[18] Y. Hong, Y. Jiang, C. Li, W. Fan, X. Yan, M. Yan, W. Shi, In-situ synthesis of direct solid-state Z-scheme V_2O_5/g-C_3N_4 heterojunctions with enhanced visible light efficiency in photocatalytic degradation of pollutants, Appl. Catal. B Environ. 180 (2016) 663–673. doi:10.1016/j.apcatb.2015.06.057.

[19] K.M. Lee, C.W. Lai, K.S. Ngai, J.C. Juan, Recent developments of zinc oxide based photocatalyst in water treatment technology: A review, Water Res. 88 (2016) 428–448. doi:10.1016/j.watres.2015.09.045.

[20] W. Yu, J. Zhang, T. Peng, New insight into the enhanced photocatalytic activity of N-, C- and S-doped ZnO photocatalysts, Appl. Catal. B Environ. 181 (2016) 220–227. doi:10.1016/j.apcatb.2015.07.031.

[21] S. Rajendran, M.M. Khan, F. Gracia, J. Qin, V.K. Gupta, S. Arumainathan, Ce^{3+}-ion-induced visible-light photocatalytic degradation and electrochemical activity of ZnO/CeO_2 nanocomposite, Sci. Rep. 6 (2016) 31641. doi:10.1038/srep31641.

[22] J. Elias, M. Bechelany, I. Utke, R. Erni, D. Hosseini, J. Michler, L. Philippe, Urchin-inspired zinc oxide as building blocks for nanostructured solar cells, Nano Energy. 1 (2012) 696–705. doi:10.1016/j.nanoen.2012.07.002.

[23] K.S. Ranjith, R.B. Castillo, M. Sillanpaa, R.T. Rajendra Kumar, Effective shell wall thickness of vertically aligned ZnO-ZnS core-shell nanorod arrays on visible photocatalytic and photo sensing properties, Appl. Catal. B Environ. 237 (2018) 128–139. doi:10.1016/j.apcatb.2018.03.099.

[24] A. Elhalil, R. Elmoubarki, M. Farnane, A. Machrouhi, F.Z. Mahjoubi, M. Sadiq, S. Qourzal, N. Barka, Synthesis, characterization and efficient photocatalytic activity of novel Ca/ZnO-Al_2O_3 nanomaterial, Mater. Today Commun. 16 (2018) 194–203. doi:10.1016/j.mtcomm.2018.06.005.

[25] V. Vaiano, M. Matarangolo, J.J. Murcia, H. Rojas, J.A. Navío, M.C. Hidalgo, Enhanced photocatalytic removal of phenol from aqueous solutions using ZnO modified with Ag, Appl. Catal. B Environ. 225 (2018) 197–206. doi:10.1016/j.apcatb.2017.11.075.

[26] P. She, K. Xu, S. Yin, Y. Shang, Q. He, S. Zeng, H. Sun, Z. Liu, Bioinspired self-standing macroporous Au/ZnO sponges for enhanced photocatalysis, J. Colloid Interface Sci. 514 (2018) 40–48. doi:10.1016/j.jcis.2017.12.003.

[27] S. Chen, J. Li, J. Bai, L. Xia, Y. Zhang, L. Li, Q. Xu, B. Zhou, Electron blocking and hole extraction by a dual-function layer for hematite with enhanced photoelectrocatalytic performance, Appl. Catal. B Environ. 237 (2018) 175–184. doi:10.1016/j.apcatb.2018.05.

[28] A.S. Alshammari, L. Chi, X. Chen, A. Bagabas, D. Kramer, A. Alromaeh, Z. Jiang, Visible-light photocatalysis on C-doped ZnO derived from polymer-assisted pyrolysis, RSC Adv. 5 (2015) 27690–27698. doi:10.1039/c4ra17227b. 068.

[29] X.X. Yu, Y. Wu, B. Dong, Z.F. Dong, X. Yang, Journal of Photochemistry and Photobiology A : Chemistry Enhanced solar light photocatalytic properties of ZnO nanocrystals by Mg-doping via polyacrylamide polymer method, J. Photoch. Photobio. A. 356 (2016) 681–688. doi:10.1016/j.jphotochem.2016.05.006.

[30] A.D. Sekar, H. Muthukumar, N.I. Chandrasekaran, M. Matheswaran, Photocatalytic degradation of naphthalene using calcined Fe–ZnO/ PVA nanofibers, Chemosphere. 205 (2018) 610–617. doi:10.1016/j.chemosphere.2018.04.131.

[31] Y. Zong, Z. Li, X. Wang, J. Ma, Y. Men, Synthesis and high photocatalytic activity of Eu-doped ZnO nanoparticles, Ceram. Int. 40 (2014) 10375–10382. doi:10.1016/j.ceramint.2014.02.123.

[32] R. Ghomri, M.N. Shaikh, M.I. Ahmed, W. Song, W. Cai, M. Bououdina, M. Ghers, Pure and (Er, Al) co-doped ZnO nanoparticles: synthesis, characterization, magnetic and photocatalytic properties, J. Mater. Sci. Mater. Electron. 29 (2018) 10677–10685. doi:10.1007/s10854-018-9136-7.

[33] Y. Liu, L. Yu, Y. Hu, C. Guo, F. Zhang, X. Wen Lou, A magnetically separable photocatalyst based on nest-like γ-Fe_2O_3/ZnO double-shelled hollow structures with enhanced photocatalytic activity, Nanoscale. 4 (2012) 183–187. doi:10.1039/c1nr11114k.

[34] J. Jadhav, S. Biswas, Hybrid ZnO:Ag core-shell nanoparticles for wastewater treatment: Growth mechanism and plasmonically enhanced photocatalytic activity, Appl. Surf. Sci. 456 (2018) 49–58. doi:10.1016/j.apsusc.2018.06.028.

[35] N. Li, J. Zhang, Y. Tian, J. Zhao, J. Zhang, W. Zuo, Precisely controlled fabrication of magnetic 3D γ-Fe_2O_3@ZnO core-shell photocatalyst with enhanced activity: Ciprofloxacin degradation and mechanism insight, Chem. Eng. J. 308 (2017) 377–385. doi:10.1016/j.cej.2016.09.093.

[36] S. Fabbiyola, V. Sailaja, L.J. Kennedy, M. Bououdina, J. Judith Vijaya, Optical and magnetic properties of Ni-doped ZnO nanoparticles, J. Alloys Compd. 694 (2017) 522–531. doi:10.1016/j.jallcom.2016.10.022.

[37] A. Kar , S. Sain, S. Kundu, A. Bhattacharyya, S. Kumar Pradhan, A. Patra, Influence of Size and Shape on the Photocatalytic Properties of SnO_2 Nanocrystals, ChemPhysChem. 16 (2015) 1017–1025. doi:10.1002/cphc.201402864.

[38] A. Ibhadon, P. Fitzpatrick, Heterogeneous Photocatalysis: Recent Advances and Applications, Catalysts. 3 (2013) 189–218. doi:10.3390/catal3010189.

[39] C. Sanchez, H. Arribart, M.M. Giraud-Guille, Biomimetism and bioinsipiration as tools for the design of innovative material and systems, Nat. Mater. 4 (2005) 277–288. doi:http://dx.doi.org/10.1038/nmat1339.

[40] I. Hashemizadeh, V.B. Golovko, J. Choi, D.C.W. Tsang, A.C.K. Yip, Photocatalytic reduction of CO_2 to hydrocarbons using bio-templated porous TiO_2 architectures under UV and visible light, Chem. Eng. J. 347 (2018) 64–73. doi:10.1016/j.cej.2018.04.094.

[41] A. Gonzalez-Perez, K.M. Persson, Bioinspired materials for water purification, Materials (Basel). 9 (2016) 447. doi:10.3390/ma9060447.

[42] C. Wang, Y. Wu, J. Lu, J. Zhao, J. Cui, X. Wu, Y. Yan, P. Huo, Bioinspired Synthesis of Photocatalytic Nanocomposite Membranes Based on Synergy of Au-TiO_2 and Polydopamine for Degradation of Tetracycline under Visible Light, ACS Appl. Mater. Interfaces. 9 (2017) 23687–23697. doi:10.1021/acsami.7b04902.

[43] V.M. Guérin, J. Elias, T.T. Nguyen, L. Philippe, T. Pauporté, Ordered networks of ZnO-nanowire hierarchical urchin-like structures for improved dye-sensitized solar cells, Phys. Chem. Chem. Phys. 14 (2012) 12948–12955. doi:10.1039/c2cp42085f.

[44] P. Sathe, K. Laxman, M.T.Z. Myint, S. Dobretsov, J. Richter, J. Dutta, Bioinspired nanocoatings for biofouling prevention by photocatalytic redox reactions, Sci. Rep. 7 (2017) 3624. doi:10.1038/s41598-017-03636-6.

[45] R.D. Campbell, Describing the shapes of fern leaves: A fractal geometrical approach, Acta Biotheoretica 44 (1996) 119-142. doi:10.1007/BF00048419

[46] L. V. Thekkekara, M. Gu, Bioinspired fractal electrodes for solar energy storages. Sci. Rep. 7 (2017) 45585. doi: 10.1038/srep45585.

[47] Q.L. Ma, R. Xiong, B.G. Zhai, Y.M. Huang, Ultrasonic synthesis of fern-like ZnO nanoleaves and their enhanced photocatalytic activity, Appl. Surf. Sci. 324 (2015) 842–848. doi:10.1016/j.apsusc.2014.11.054.

[48] Y. Wang, C.-G. Niu, L. Wang, Y. Wang, X.-G. Zhang, G.-M. Zeng, Synthesis of fern-like Ag/AgCl/$CaTiO_3$ plasmonic photocatalysts and their enhanced visible-light photocatalytic properties, RSC Adv. 6 (2016) 47873–47882. doi:10.1039/C6RA06435C.

[49] A.A. Ibrahim, A. Umar, R. Kumar, S.H. Kim, A. Bumajdad, S. Baskoutas, Sm_2O_3-doped ZnO beech fern hierarchical structures for nitroaniline chemical sensor, Ceram. Int. 42 (2016) 16505–16511. doi:10.1016/j.ceramint.2016.07.061.

[50] T. Sen, N.G. Shimpi, S. Mishra, R. Sharma, Sensors and Actuators B : Chemical Polyaniline/α-Fe_2O_3 nano-composite for room temperature LPG sensing, Sensors Actuators B. Chem. 190 (2014) 120–126. doi:10.1016/j.snb.2013.07.091.

[51] C. E. Sabel, J. M. Neureuther, S. Siemann, A spectrophotometric method for the determination of zinc, copper, and cobalt ions in metalloproteins using Zincon, Anal. Biochem. 397 (2010) 218-226. doi:10.1016/j.ab.2009.10.037.

[52] C. Anastasescu, C. Negrila, D. G. Angelescu, I. Atkinson, M. Anastasescu, N. Spataru, M. Zaharescu, I. Balint, Particularities of photocatalysis and formation of reactive oxygen species on insulators and semi-conductors: cases of SiO_2, TiO_2 and their composite SiO_2–TiO_2, Catal. Sci. Technol., 8 (2018) 5657-5668. doi: 10.1039/C8CY00991K.

[53] M. Skompska, K. Zarębska, Electrodeposition of ZnO nanorod arrays on transparent conducting substrates-a review, Electrochim. Acta. 127 (2014) 467–488. doi:10.1016/j.electacta.2014.02.049.

[54] O. Lupan, V.M. Guérin, I.M. Tiginyanu, V. V. Ursaki, L. Chow, H. Heinrich, T. Pauporté, Well-aligned arrays of vertically oriented ZnO nanowires electrodeposited on ITO-coated glass and their integration in dye sensitized solar cells, J. Photochem. Photobiol. A Chem. 211 (2010) 65–73. doi:10.1016/j.jphotochem.2010.02.004.

[55] V.M. Guérin, T. Pauporté, From nanowires to hierarchical structures of template-free electrodeposited ZnO for efficient dye-sensitized solar cells, Energy Environ. Sci. 4 (2011) 2971–2979. doi:10.1039/c1ee01218e.

[56] M. Law, L.E. Greene, J.C. Johnson, R. Saykally, P. Yang, Nanowire dye-sensitized solar cells, Nat. Mater. 4 (2005) 455–459. doi:10.1038/nmat1387.

[57] F. Gazette, Recent advances in the understanding of fern responses to light, Fern Gaz. 19 (2013) 97–115.

[58] R. Al-Gaashani, S. Radiman, A.R. Daud, N. Tabet, Y. Al-Douri, XPS and optical studies of different morphologies of ZnO nanostructures prepared by microwave methods, Ceram. Int. 39 (2013) 2283–2292. doi:10.1016/j.ceramint.2012.08.075.

[59] J.H. Zheng, Q. Jiang, J.S. Lian, Synthesis and optical properties of flower-like ZnO nanorods by thermal evaporation method, Appl. Surf. Sci. 257 (2011) 5083–5087. doi:10.1016/j.apsusc.2011.01.025.

[60] J. Das, S.K. Pradhan, D.R. Sahu, D.K. Mishra, S.N. Sarangi, B.B. Nayak, S. Verma, B.K. Roul, Micro-Raman and XPS studies of pure ZnO ceramics, Phys. B 405 (2010) 2492–2497. doi:10.1016/j.physb.2010.03.020.

[61] W.J. Liu, X.D. Tang, Z. Tang, W. Bai, N.Y. Tang, Oxygen defects mediated magnetism of Ni doped ZnO, Adv. Condens. Matter Phys. 2013 (2013) 424398. doi:10.1155/2013/424398.

[62] H.W. Nesbitt, D. Legrand, G.M. Bancroft, Interpretation of Ni2p XPS spectra of Ni conductors and Ni insulators, Phys. Chem. Miner. 27 (2000) 357–366. doi:10.1007/s002690050265.

[63] S. Husain, F. Rahman, N. Ali, P.A. Alvi, Nickel Sub-lattice Effects on the Optical Properties of ZnO Nano-crystals, J. Optoelectron. Eng. 1 (2013) 28–32. doi:10.12691/joe-1-1-5.

[64] B.D. Viezbicke, S. Patel, B.E. Davis, D.P. Birnie, Evaluation of the Tauc method for optical absorption edge determination: ZnO thin films as a model system, Phys. Status Solidi B Basic Res. 252 (2015) 1700–1710. doi:10.1002/pssb.201552007.

[65] J.B. Coulter, D.P. Birnie, Assessing Tauc Plot Slope Quantification: ZnO Thin Films as a Model System, Phys. Status Solidi B Basic Res. 255 (2018) 1700393. doi:10.1002/pssb.201700393.

[66] A. Torabi, V. N. Staroverov, Band gap reduction in ZnO and ZnS by creating layered ZnO/ZnS heterostruc-tures, J. Phys. Chem. Lett. 6 (2015) 2075–2080. doi: 10.1021/acs.jpclett.5b00687

[67] L.V. Trandafilović, D.J. Jovanović, X. Zhang, S. Ptasińska, M.D. Dramićanin, Enhanced photocatalytic degradation of methylene blue and methyl orange by ZnO:Eu nanoparticles, Appl. Catal. B Environ. 203 (2017) 740–752. doi:10.1016/j.apcatb.2016.10.063.

[68] C. Dong, X. Xiao, G. Chen, H. Guan, Y. Wang, Synthesis and photocatalytic degradation of methylene blue over p-n junction Co_3O_4/ZnO core/shell nanorods, Mater. Chem. Phys. 155 (2015) 1–8. doi:10.1016/j.matchemphys.2015.01.033.

[69] Q. Jiaqian, Z. Xinyu, Y. Chengwu, C. Meng, M. Mingzhen, L. Riping, ZnO microspheres-reduced graphene oxide nanocomposite for photocatalytic degradation of methylene blue dye, Appl. Surf. Sci. 392 (2016) 196–203.

[70] N. Liu, Z. Li, Bimetal-organic frameworks derived carbon doped ZnO/Co_3O_4 heterojunction as visible-light stabilized photocatalysts, Mater. Sci. Semicond. Process. 79 (2018) 24–31. doi:10.1016/j.mssp.2018.01.004.

[71] M.F. Sanad, A.E. Shalan, S.M. Bazid, S.M. Abdelbasir, Pollutant degradation of different organic dyes using the photocatalytic activity of ZnO@ZnS nanocomposite materials, J. Environ. Chem. Eng. 6 (2018) 3981–3990. doi:10.1016/j.jece.2018.05.035.

[72] M. Aslam, I.M.I. Ismail, T. Almeelbi, N. Salah, S. Chandrasekaran, A. Hameed, Enhanced photocatalytic activity of V_2O_5-ZnO composites for the mineralization of nitrophenols, Chemosphere. 117 (2014) 115–123. doi:10.1016/j.chemosphere.2014.05.076.

[73] R. Yousefi, F. Jamali-Sheini, M. Cheraghizade, S. Khosravi-Gandomani, A. Sáaedi, N.M. Huang, W.J. Basirun, M. Azarang, Enhanced visible-light photocatalytic activity of strontium-doped zinc oxide nanoparticles, Mater. Sci. Semicond. Process. 32 (2015) 152–159. doi:10.1016/j.mssp.2015.01.013.

[74] M.T. Qamar, M. Aslam, I.M.I. Ismail, N. Salah, A. Hameed, Synthesis, characterization, and sunlight mediated photocatalytic activity of CuO coated ZnO for the removal of nitrophenols, ACS Appl. Mater. Interfaces. 7 (2015) 8757–8769. doi:10.1021/acsami.5b01273.

[75] M.T. Uddin, Y. Nicolas, C. Olivier, L. Servant, T. Toupance, S. Li, A. Klein, W. Jaegermann, Improved photocatalytic activity in RuO_2-ZnO nanoparticulate heterostructures due to inhomogeneous space charge effects, Phys. Chem. Chem. Phys. 17 (2015) 5090–5102. doi:10.1039/c4cp04780j.

[76] S. Verma, R.K. Dutta, Enhanced ROS generation by ZnO-ammonia modified graphene oxide nanocomposites for photocatalytic degradation of trypan blue dye and 4-nitrophenol, J. Environ. Chem. Eng. 5 (2017) 4776–4787. doi:10.1016/j.jece.2017.08.026.

[77] M. Rabbani, M. Heidari-Golafzani, R. Rahimi, Synthesis of TCPP/$ZnFe_2O_4$@ZnO nanohollow sphere composite for degradation of methylene blue and 4-nitrophenol under visible light, Mater. Chem. Phys. 179 (2016) 35–41. doi:10.1016/j.matchemphys.2016.05.005.

[78] H. Mou, C. Song, Y. Zhou, B. Zhang, D. Wang, Design and synthesis of porous Ag/ZnO nanosheets assemblies as super photocatalysts for enhanced visible-light degradation of 4-nitrophenol and hydrogen evolution, Appl. Catal. B Environ. 221 (2018) 565–573. doi:10.1016/j.apcatb.2017.09.061.

[79] S. Akir, A. Barras, Y. Coffinier, M. Bououdina, R. Boukherroub, A.D. Omrani, Eco-friendly synthesis of ZnO nanoparticles with different morphologies and their visible light photocatalytic performance for the degradation of Rhodamine B, Ceram. Int. 42 (2016) 10259–10265. doi:10.1016/j.ceramint.2016.03.153.

[80] J. Wang, J. Yang, X. Li, B. Feng, B. Wei, D. Wang, H. Zhai, H. Song, Effect of surfactant on the morphology of ZnO nanopowders and their application for photodegradation of rhodamine B, Powder Technol. 286 (2015) 269–275. doi:10.1016/j.powtec.2015.08.030.

[81] Y. Zhang, J. Zhou, Z. Li, Q. Feng, Photodegradation pathway of rhodamine B with novel Au nanorods@ZnO microspheres driven by visible light irradiation, J. Mater. Sci. 53 (2018) 3149–3162. doi:10.1007/s10853-017-1779-x.

[82] J. Chen, W. Liao, Y. Jiang, D. Yu, M. Zou, H. Zhu, M. Zhang, M. Du, Facile Fabrication of ZnO/TiO_2 Heterogeneous Nanofibres and Their Photocatalytic Behaviour and Mechanism towards Rhodamine B, Nanomater. Nanotechnol. 6 (2016) 9. doi:10.5772/62291.

[83] N. Rana, S. Chand, A.K. Gathania, Synthesis and characterization of flower-like ZnO structures and their applications in photocatalytic degradation of Rhodamine B dye, J. Mater. Sci. Mater. Electron. 27 (2016) 2504–2510. doi:10.1007/s10854-015-4051-7.

[84] H. Zhai, L. Wang, D. Sun, D. Han, B. Qi, X. Li, L. Chang, J. Yang, Direct sunlight responsive Ag-ZnO heterostructure photocatalyst: Enhanced degradation of rhodamine B, J. Phys. Chem. Solids. 78 (2015) 35–40. doi:10.1016/j.jpcs.2014.11.004.

[85] P. Nuengmatcha, S. Chanthai, R. Mahachai, W.C. Oh, Visible light-driven photocatalytic degradation of rhodamine B and industrial dyes (texbrite BAC-L and texbrite NFW-L) by ZnO-graphene-TiO_2 composite, J. Environ. Chem. Eng. 4 (2016) 2170–2177. doi:10.1016/j.jece.2016.03.045.

[86] M. Pirhashemi, A. Habibi-Yangjeh, Facile fabrication of novel ZnO/$CoMoO_4$ nanocomposites: Highly efficient visible-light-responsive photocatalysts in degradations of different contaminants, J. Photochem. Photobiol. A Chem. 363 (2018) 31–43. doi:10.1016/j.jphotochem.2018.05.027.